Optimizing the Biogeochemical Argo Float Distribution

PAUL CHAMBERLAIN[a] LYNNE D. TALLEY,[a] BRUCE CORNUELLE,[a] MATTHEW MAZLOFF,[a] AND SARAH T. GILLE[a]

[a] University of California, San Diego, La Jolla, California

ABSTRACT: The core Argo array has operated with the design goal of uniform spatial distribution of 3° in latitude and longitude. Recent studies have acknowledged that spatial and temporal scales of variability in some parts of the ocean are not resolved by 3° sampling and have recommended increased core Argo density in the equatorial region, boundary currents, and marginal seas with an integrated vision of other Argo variants. Biogeochemical (BGC) Argo floats currently observe the ocean from a collection of pilot arrays, but recently funded proposals will transition these pilot arrays to a global array. The current BGC Argo implementation plan recommends uniform spatial distribution of BGC Argo floats. For the first time, we estimate the effectiveness of the existing BGC Argo array to resolve the anomaly from the mean using a subset of modeled, full-depth BGC fields. We also study the effectiveness of uniformly distributed BGC Argo arrays with varying float densities at observing the ocean. Then, using previous Argo trajectories, we estimate the Argo array's future distribution and quantify how well it observes the ocean. Finally, using a novel technique for sequentially identifying the best deployment locations, we suggest the optimal array distribution for BGC Argo floats to minimize objective mapping uncertainty in a subset of BGC fields and to best constrain BGC temporal variability.

KEYWORDS: Ocean; In situ oceanic observations; Optimization; Semi-Lagrangian models; Oceanic variability

1. Introduction

Once a distant prospect, research infrastructure funding is providing a 5-yr opportunity to procure and deploy a global array of Biogeochemical (BGC) Argo floats. For the first time, nitrate, oxygen, chlorophyll, and pH will be measured on a global scale in near–real time and will provide insight into how BGC variables flux and ventilate the ocean (Majkut et al. 2014; Landschützer et al. 2016; Bushinsky et al. 2019, 2017).

The core Argo array collects temperature and salinity profiles throughout most of the open ocean. For over 20 years, core Argo floats have been deployed at locations to achieve or exceed uniform spatial coverage of 3° latitude × 3° longitude (Roemmich et al. 1999). Recent Argo analysis has recognized that there exists higher temperature and salinity variability in specific regions and has called for doubled Argo density in the tropics, marginal seas, and boundary currents as part of the new One Argo global design (Roemmich et al. 2019).

One Argo consists of three components: core Argo, Deep Argo, and BGC Argo. The six BGC sensors specified for the newly developing BGC Argo component are oxygen, nitrate, pH (used to constrain the carbonate system), fluorescence (converted to chlorophyll concentration), backscatter, and downwelling irradiance. BGC Argo floats in One Argo follow the same profiling mission as core Argo floats: profiling to 2000 m every 10 days and parking at 1000 m between profiles. BGC Argo float density has been specified at about one quarter the density of core Argo (Johnson and Claustre 2016), for a total of about 1000 floats globally. The growing global BGC Argo array is currently a collection of pilot arrays (Fig. 1). The largest of these is the Southern Ocean Carbon and Climate Observations and Modeling (SOCCOM) project, which maintains

about 120 BGC floats in the Southern Ocean (Johnson et al. 2017). To bridge the gaps between pilot arrays, a new U.S. project called GO-BGC is deploying 500 floats globally.

The BGC Argo Science and Implementation Plan (Johnson and Claustre 2016) guides the design goals of the global BGC array. After some analysis of the spatial and temporal variability of BGC fields, Johnson and Claustre (2016) state "It was, therefore, concluded that initial deployments and operations should begin with the premise that a relatively uniform distribution of floats was adequate. Again, this assumption will be tested as more experience is obtained." Several studies have considered BGC Argo array design and give insight on the uniform distribution assumption made in Johnson and Claustre (2016). In a seminal BGC Argo study and motivating study for Johnson and Claustre, Majkut et al. (2014) estimated the uncertainty of CO_2 flux estimates in the Southern Ocean that can be inferred using modeled surface fields and a hypothetical, uniformly distributed array of Argo floats. These estimates are surface restricted, do not consider the cross covariance with other observations, and use stationary floats for calculating estimates. Johnson and Claustre extended Majkut et al.'s work, estimating the amount of global CO_2 flux that a hypothetical, uniformly distributed array of 500, 1000, and 2000 floats could constrain; the study considers other factors such as chlorophyll variability and decorrelation length scales and ultimately concludes that 1000 floats is an appropriate BGC Argo density. However, the Johnson and Claustre analysis is subject to the same limitations of being surface restricted, not considering the full effects of all BGC sensors, and using stationary floats. Ford (2021) considered the improvements to BGC reanalysis using a full-depth multivariable model. Ford simulated initial float location and movement based on an amalgamation of actual float trajectories taken from 2009 to 2011, modifying their distribution to achieve the hypothetical design goals. This study found a synergistic effect

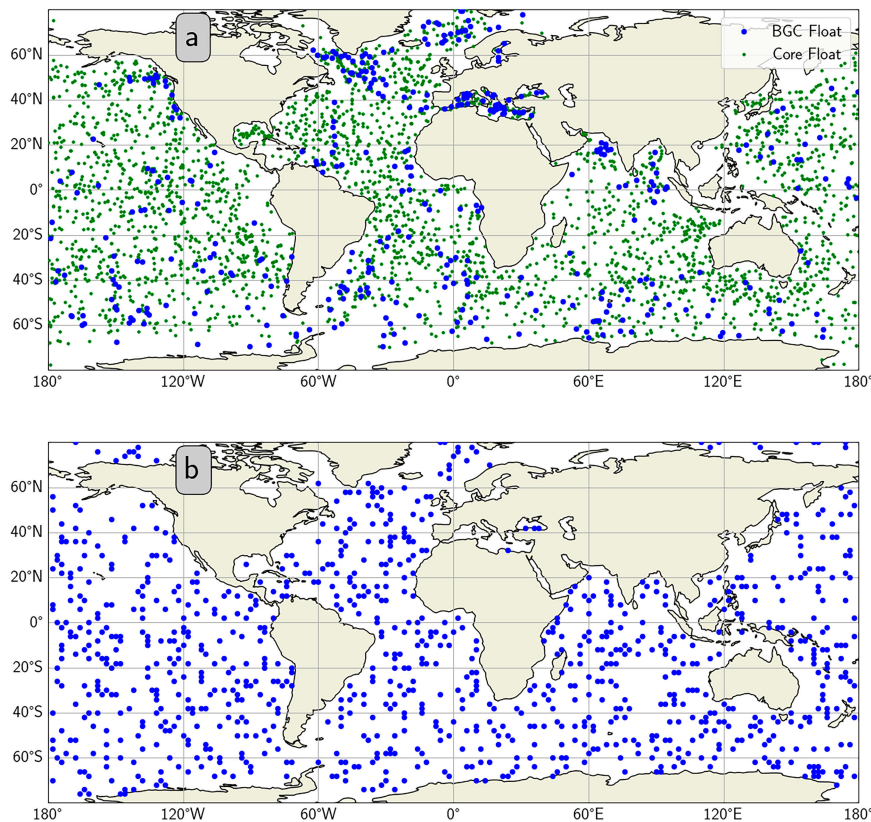Corresponding author: Paul Chamberlain, pchamber@ucsd.edu

FIG. 1. (a) Map of May 2021 snapshot Core and BGC Argo floats and (b) example of random BGC float locations. Green dots are core Argo floats, and blue dots are BGC floats.

of multiple BGC variables in improving assimilated model BGC performance (likely attributable to the covariance between BGC variables) and suggested that a BGC Argo array larger than 1000 floats may be appropriate. Kamenkovich et al. (2017) advected floats using full-depth HYCOM reanalysis model velocity fields from 2010 to 2014, with complete BGC fields, to study the impact of BGC floats on Southern Ocean observing systems.

These studies can be incrementally improved to a greater or lesser degree in several ways: (i) include an estimate of float motion, (ii) quantify the impact of the BGC array at depths to 2000 m because an observing system designed for one depth level may not be suitable for all, and (iii) consider the strong cross covariances that exist between BGC variables and temperature and salinity because the observation of one variable can constrain a significant amount of variance in another (Fig. 2 shows the correlation of temperature BGC variables with oxygen and chlorophyll—salinity and pH correlations with temperature are not shown but show similar patterns). A float can travel a substantial distance over its lifespan. If not accounted for, this float motion can produce biases in the spatial distribution of the array and assimilation products that use these data (Kamenkovich et al. 2011). The spatial distribution of variability and the amplitude and phases of the seasonal cycles are different for each BGC variable (Fig. 3e). Designing an array to capture one variable may

not adequately constrain all of the others. The spatial scales of BGC covariance are large in the surface ocean: as illustrated in Fig. 2, which shows the strong cross covariances of chlorophyll, temperature, and oxygen at the near surface. Comparing the gravest eigenmodes of pH covariance for two different depths (Figs. 4 and 5) reveals that the spatial scales of BGC covariance are largest in the upper ocean. Many important and open climate monitoring results, like understanding the change of bulk inventories of oxygen or carbon at depth, need data of an appropriate spatial density to estimate processes and inventories at depth accurately.

The observing system design method that we present has three components. First, we use a transition matrix operator to predict future float locations. Our Argo-specific transition matrix, documented in a companion publication (Chamberlain et al. 2023), is a statistical construction derived from Argo float trajectory histories that can be used to propagate an array into the future. Second, we use the coupled, full ocean depth Global Climate Model CM4 (Held et al. 2019; Adcroft et al. 2019; Dunne et al. 2020) to generate the statistics used in our observing system experiments. CM4 calculates temperature and salinity, chlorophyll, pH, and oxygen and does not calculate nitrate, backscatter, or downwelling irradiance; BGC Argo floats measure all these variables. Finally, we use BGC cross covariances calculated from CM4 to account for the additional constraint that the measurement of a covarying variable has on the amount
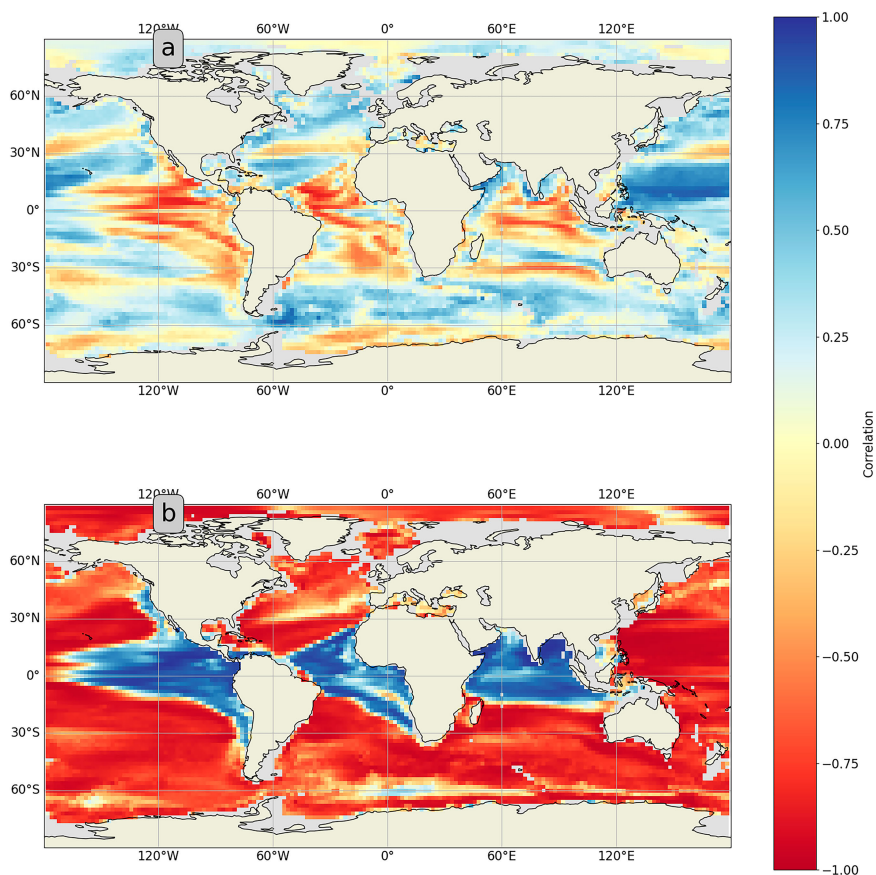
FIG. 2. Global climate model (CM4) (Held et al. 2019; Adcroft et al. 2019; Dunne et al. 2020) correlation maps of (a) chlorophyll and oxygen and (b) temperature and oxygen at a depth of 100 m. Colored shading represents strength of correlation. Beige shading represents land. Gray areas are too shallow to be calculated in simulations.

of BGC variance constrained by the observing system. In our calculations, we consider the variance constrained by both core and BGC Argo floats.

In this study, we optimize the float array spatial distribution to constrain the maximum amount of temporal variance of modeled variables over several depths. Observations and assumptions from the resulting float array are best suited to observe the temporal variability given the criteria of the calculation. By construction, as compared to other float distributions, the observations from the optimized array can be used to create large-scale objective maps with the smallest uncertainty in the anomaly from the mean or to constrain data assimilating models with minimum error covariance.

However, in addition to the homogeneous distributions of One Argo and the methods explained here, many other criteria can define an optimal distribution. Observing system design experiments by Kamenkovich et al. (2017) have quantified how well arrays resolve the seasonal climatology of BGC variables. While seasonal variability is the dominant mode of variability we observe, the optimal array we present may not be ideal for observing this signal. Time of emergence studies (Schlunegger et al. 2020) have estimated where, when, and how anthropogenic

climate change can be detected. An array of floats could be designed to optimally quantify the anthropogenic signal by increasing the density of observations where the anthropogenic BGC signal will appear first and be most pronounced; however, our method is not optimized for detecting this signal. Indeed, because our methods assume stationary statistics, the proposed array may not observe the effects of climate change as rapidly as an array designed to achieve that goal.

Argo floats sample at 10-day intervals; this is not ideal to observe high-frequency surface fluxes (Monteiro et al. 2015). With the advent of efficient two-way satellite communication to Argo floats via Iridium, one can imagine a network of floats with regionally or seasonally adaptive temporal sampling to capture higher-frequency signals in certain BGC provinces (Reygondeau et al. 2013). Optimal temporal sampling is an important and open question. This study only addresses spatial sampling using spatial covariances and assumes that uncertainty or biases from sampling at too low a frequency can be represented by increasing the assumed uncertainty of observations.

Finally, previous studies have documented unique BGC provinces (Fay and McKinley 2014) and compelling BGC
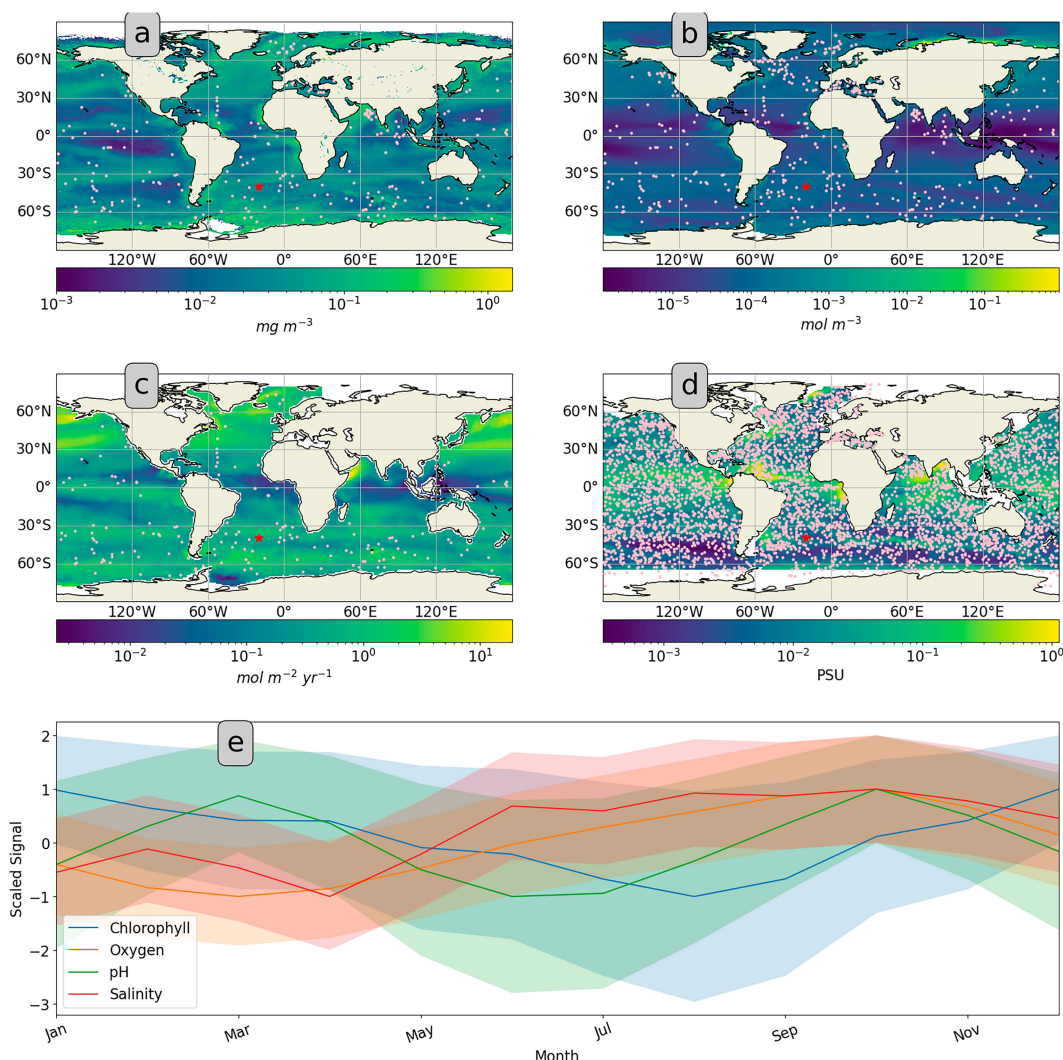
FIG. 3. (a)–(d) Maps of standard deviation of (a) chlorophyll (NASA 2022), (b) oxygen (CM4), (c) CO_2 flux (Landschützer et al. 2016), and (d) salinity (Roemmich and Gilson 2009). Pink dots represent deployed floats with a sensor equipped to measure (a) chlorophyll, (b) oxygen, (c) pH, and (d) salinity. Colored shading represents the standard deviation of the variable. Beige shading is land. (e) Monthly mean and anomaly from annual mean normalized by standard deviation from CM4 for chlorophyll (blue line), oxygen (orange line), pH (green line), and salinity (red line) at 40°S, 20°W (denoted by red star on all maps).

phenomena observed from BGC floats (Campbell et al. 2019; Prend et al. 2019). The proposed deployment methods are not optimized to observe these regional phenomena that have large-scale climate impacts. Skilled Argo deployment managers will always be required to tailor deployments to specific regional circumstances, but the optimization can provide a skilled initial estimate.

In summary, we accept the challenge posed by Johnson and Claustre (2016) to go beyond uniform float distribution and explore regionally optimized float density. The analysis we show is just one possibility. It is difficult to predict the future scientific needs of the Argo program. Therefore, we present a framework for location selection that, through either models or community consensus, future biogeochemical researchers

can use to produce optimal float deployments. Bretherton et al. (1976), who provided the intellectual genesis for much of this work, said this more succinctly: "no refinement of analysis will eliminate the need for caution tempered by judgement in the application of these methods to the designs of major programmes." We push forward with their ethos.

2. Data

a. Argo float data

The analysis presented here requires Argo float locations and sensor suites. For this study, Argo float locations were taken from the May 2021 Argo snapshot (Argo 2021). Argo floats are intentionally staggered so that not all floats profile
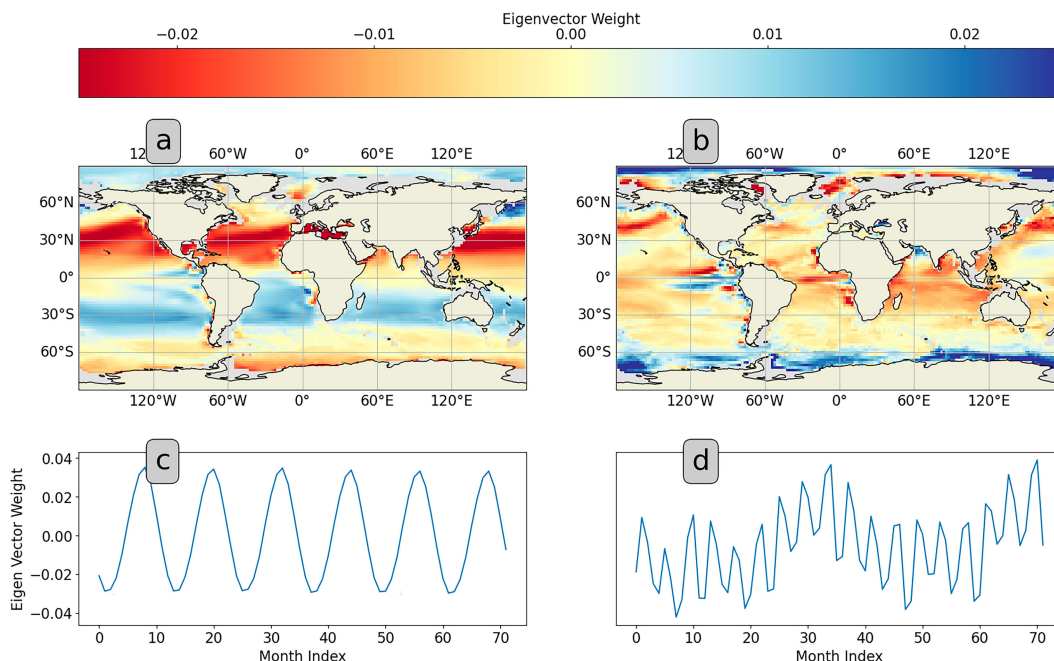
FIG. 4. (a),(b) CM4 maps of eigenvectors of spatial surface pH covariance for (a) the gravest mode and (b) the seventh eigenmode. Colored shading represents the covariance weighting, and beige shading indicates land. (c),(d) 72-month subsets of eigenvectors of temporal surface pH covariance for (c) the gravest mode and (d) the seventh eigenmode. Gravest mode explains 14.0% of the variance, and seventh eigenmode explains 0.8% of the variance. The first and seventh eigenmodes are shown as an example to explain the scaling argument of section 3c.

on the same day. We used the most recently reported positions of the active Argo floats; for this analysis, Argo floats were considered active if they had reported a position during the previous 6 months. With the advent of BGC Argo, not all Argo floats carry the same sensor suite. BGC Argo data are hosted by the Argo Global Data Acquisition Centers (GDACs), and the specific sensor makeup of each float was available in the downloaded GDAC snapshot (Figs. 1 and 3).

b. Biogeochemical model

We used the CM4 coupled ocean–atmosphere model (Held et al. 2019; Adcroft et al. 2019) to estimate the spatial covariance of global ocean biogeochemistry. The CM4 ocean has a nominal grid spacing of $1/4° \times 1/4°$ of latitude and longitude, and 75 depth levels with 2-m spacing at the surface and 200-m spacing at depth. CM4 ocean biogeochemistry was calculated using the Biology Light Iron Nutrient and Gas (BLINGv2) model (Galbraith et al. 2010; Dunne et al. 2020). The surface and subsurface biogeochemical model results compare well with observations; however, BLINGv2 is, by design, unable to distinguish between the phosphorus and nitrogen nutrient cycles and is also sensitive to spurious results in the physical processes of CM4—specifically increased ventilation in the southern midlatitudes. These calculations used the daily averaged model temperature, salinity, oxygen, pH, and chlorophyll from 1850 to 2009. We reduced the computational burden by subsampling CM4 to a grid spacing of $2° \times 2°$ of latitude and longitude where depths are greater than 2000 m. Depth levels of 15, 40, 87.5, 137.5, 225, 350, 550, 750, 950,

1150, 1350, 1625, and 2250 m were used in these calculations. Chlorophyll was only calculated in the euphotic zone, which we define as all depths equal to or shallower than 137.5 m, and the logarithm of chlorophyll was used in these calculations as is standard practice (Campbell 1995). In total, the spatial domain of each depth level contained 9059 distinct grid cells of latitude and longitude extending from 76°S to 88°N. Over all depth levels and across all variables, the model data comprised 507 304 individual time series.

c. Transition matrix

A transition matrix is an operator that propagates a state vector forward or backward in time. In this case, the transition matrix is calculated from previous Argo trajectories to propagate the Argo float array through time. The Argo float array is represented in these calculations as the Argo state vector, which exists in the spatial grid defined by the Argo state space. This spatial grid is a subset of the CM4 $2° \times 2°$ latitude and longitude spatial grid and defines all the locations in the ocean that an Argo float can occupy. (Some areas, like the Arctic, do not have many Argo trajectories, and those grid cells were excluded from the transition matrix.) The transition matrix is a square matrix with rows and columns equal to the size of the Argo state space and defines the transitions of a discrete-time Markov chain. The transition matrix we use has a 90-day time step. The details of construction of this transition matrix and choices of this gridcell size and time step can be found in Chamberlain et al. (2023).
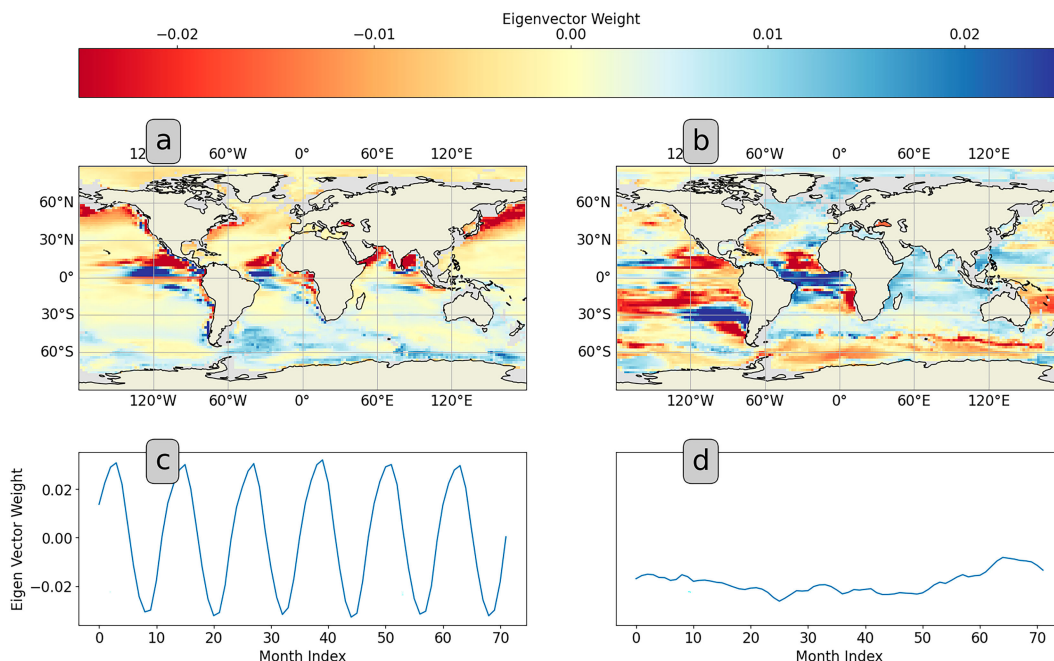
FIG. 5. (a),(b) CM4 maps of eigenvectors of spatial pH covariance for (a) the gravest mode at 100 m depth and (b) the gravest mode at 1000 m depth. Colored shading represents the covariance weighting, and beige shading indicates land. (c),(d) 72-month subsets of eigenvectors of temporal pH covariance for (c) the gravest mode at 100 m depth and (d) the gravest mode at 1000 m depth. Gravest mode at 100 m depth explains 15.5% of the variance, and gravest mode at 1000 m depth explains 6.9% of the variance.

3. Methods

In this study, we fuse two established techniques: (i) a method that quantifies the amount of variance constrained by the full sensor suite of a BGC float, based on objective mapping (Bretherton et al. 1976) using statistics generated from the CM4 model, and (ii) the transition matrix approach that statistically predicts the future location of either an individual float or an entire float array computed using all previous observed Argo trajectories (Markov 1906; Sévellec et al. 2017; Chamberlain et al. 2023). Our primary innovation is the combination of these ideas. Many of the scientific questions posed for BGC Argo arrays involve inventories and fluxes of BGC variables. Therefore, assessing the effect of a float observation has less practical utility if float planners do not know where the float will be, and, conversely, accurately predicting the observational density has less importance if the impact of observations to constrain models or budgets is unquantified (Chamberlain et al. 2018). This procedure is also applicable to core Argo properties, with of course the same transition matrix, and to other observing systems for which a transition matrix can be computed, whether from previous observations or from a model.

In section 3a, we broadly explain the objective mapping and mapping error methods that are used in this work. The literature on this topic is well developed, and a summary is provided for convenience. Objective mapping depends on knowledge of the means and covariances of the mapped fields, which require a large amount of data to calculate

accurately. In this case, we use the CM4 model output to estimate the covariances. Oceanic BGC variables have different variances and spatial and temporal scales of covariance (Fig. 3). To compare these variables, it is necessary to normalize them to be nondimensional, with sizes reflecting their importance to the analysis. The normalization factors can vary with variable type and location.

In section 3b, we describe the processing methods for the CM4 model data. We attempt to mitigate spurious covariances and reduce the computational burden of these methods by applying a localization to the covariances calculated from the normalized data. A localization is a filter that restricts the regional extent that a specific grid cell can influence. The localization used in this work is described in section 3c.

With the processed and localized data, the full covariance matrix in space is calculated for all points and variables and used to estimate mapping error for a given Argo float distribution. In section 3d we describe the method to calculate the variance constrained by a static Argo array. We consider both existing Argo locations and hypothetical random distributions. Next, we propagate Argo floats into the future using the transition matrix, computed from historical Argo trajectories, and consider the amount of variance constrained by a future float distribution in section 3e. Finally, in section 3f, we explain our method for constructing an optimal array and the testing procedures for quantifying the array's performance. The description of our methods uses the notation of Ide et al. (1997) and the processes and products described in section 3 are represented schematically in Fig. 7.

a. Objective mapping

Observations $\mathbf{y}(t)^o$ (length m) of a state vector $\mathbf{x}(t)$ are expressed as

$$\mathbf{y}(t)^o = \mathbf{H}\mathbf{x}(t) + \boldsymbol{\epsilon}, \tag{1}$$

where $\mathbf{H}$ is the linearized observation operator, $\boldsymbol{\epsilon}$ is the noise process, and the superscript o refers to observations. The state vector $\mathbf{x}(t)$ has dimension n and uncertainty covariance matrix $\mathbf{P}^b$. The noise process $\boldsymbol{\epsilon}$ of length m is assumed to have zero mean and covariance matrix $\mathbf{R}$. The noise process is composed of instrumental and representation errors.

The state vector $\mathbf{x}(t)$ contains the values of all the physical and BGC property variables from the CM4 model—temperature, salinity, oxygen, pH, and chlorophyll in the euphotic depths. The state vector can be restricted to a single depth, or can be a combination of multiple depths, and is a subset of the model grid points. This means that the number of elements (n) in the state vector $\mathbf{x}(t)$ is the number of grid points in the domain multiplied by the number of variables and depths considered: this can be many times longer than the total number of grid points in our domain. In general, including additional independent variables and depth levels provides more information about the state, but can be computationally expensive as the covariance calculation cost increases quadratically with the number of elements (n) in the state vector. We use a time series of model state $\mathbf{x}$ around its time mean to estimate the background error covariance $\mathbf{P}^b$. This is defined as

$$\mathbf{P}^b = E[\mathbf{x}\mathbf{x}^{\mathrm{T}}], \tag{2}$$

where E is the expected value and superscript T is the transform. Matrix $\mathbf{P}^b$ contains the cross covariances between biogeochemical variables across depths and grid points (Fig. 2). We assume $\mathbf{x}$ to be the true state of global biogeochemistry. Of course, CM4 has biases and uncertainties (Held et al. 2019; Dunne et al. 2020), but the exact structure of these errors is outside the scope of this analysis.

Now we search for a linear estimate of $\mathbf{x}$ from the observations $\mathbf{y}^o$. Assume there exists a $\mathbf{K}$, termed the Kalman gain, such that

$$\hat{\mathbf{x}} = \mathbf{K}\mathbf{y}^o, \tag{3}$$

where $\hat{\mathbf{x}}$ is the state estimate. The analysis error covariance $\mathbf{P}^a$ is defined as

$$\mathbf{P}^a = E[(\mathbf{x} - \hat{\mathbf{x}})(\mathbf{x} - \hat{\mathbf{x}})^{\mathrm{T}}] \tag{4}$$

$$= E[(\mathbf{x} - \mathbf{K}\mathbf{y}^o)(\mathbf{x} - \mathbf{K}\mathbf{y}^o)^{\mathrm{T}}] \tag{5}$$

$$= \mathbf{K}\mathbf{P}_{yy}\mathbf{K}^{\mathrm{T}} - \mathbf{P}_{xy}\mathbf{K}^{\mathrm{T}} - \mathbf{K}\mathbf{P}_{xy} + \mathbf{P}^b, \tag{6}$$

where $\mathbf{P}_{xy}$ is the covariance between modeled locations and observed locations (model–data covariance), and $\mathbf{P}_{yy}$ is the covariance between observed locations (data–data covariance). Matrix $\mathbf{P}^b$ [Eq. (2)] is the covariance between all elements of the state vector (model–model covariance). From Eq. (1) we have an expression for the observations, the covariance of which can be written:

$$\mathbf{P}_{yy} = E[\mathbf{y}^o\mathbf{y}^{o\mathrm{T}}] = E[(\mathbf{H}\mathbf{x} + \boldsymbol{\epsilon})(\mathbf{H}\mathbf{x} + \boldsymbol{\epsilon})^{\mathrm{T}}] = \mathbf{H}\mathbf{P}^b\mathbf{H}^{\mathrm{T}} + \mathbf{R}. \tag{7}$$

Similarly,

$$\mathbf{P}_{xy} = E[\mathbf{x}\mathbf{y}^{o\mathrm{T}}] = E[\mathbf{x}(\mathbf{H}\mathbf{x} + \boldsymbol{\epsilon})^{\mathrm{T}}] = \mathbf{P}^b\mathbf{H}^{\mathrm{T}}. \tag{8}$$

We complete the square (Saxon 2008) by adding $\mathbf{P}_{xy}\mathbf{P}_{yy}^{-1}\mathbf{P}_{xy}^{\mathrm{T}}$ to both sides of Eq. (6). This gives

$$\mathbf{P}^a = (\mathbf{K} - \mathbf{P}_{xy}\mathbf{P}_{yy}^{-1})\mathbf{P}_{yy}(\mathbf{K} - \mathbf{P}_{xy}\mathbf{P}_{yy}^{-1})^{\mathrm{T}} + \mathbf{P}^b - \mathbf{P}_{xy}\mathbf{P}_{yy}^{-1}\mathbf{P}_{xy}^{\mathrm{T}}. \tag{9}$$

If we assume the error $\boldsymbol{\epsilon}$ has zero mean and is stationary, and that the error of distinct points are uncorrelated with each other, then we can differentiate Eq. (9) to find the Kalman gain $\mathbf{K}$ that minimizes the variance of $\mathbf{P}^a$. At an extremum,

$$\frac{\delta\mathrm{tr}(\mathbf{P}^a)}{\delta\mathbf{K}} = 2(\mathbf{K} - \mathbf{P}_{xy}\mathbf{P}_{yy}^{-1})^{\mathrm{T}}\mathbf{P}_{yy} = 0, \tag{10}$$

$$\mathbf{K} = \mathbf{P}_{xy}\mathbf{P}_{yy}^{-1}, \tag{11}$$

and

$$\mathbf{P}^a = \mathbf{P}^b - \mathbf{P}_{xy}\mathbf{P}_{yy}^{-1}\mathbf{P}_{xy}^{\mathrm{T}}. \tag{12}$$

Substituting Eqs. (7) and (8) into Eqs. (11) and (12), we obtain

$$\mathbf{K} = \mathbf{P}^b\mathbf{H}^{\mathrm{T}}(\mathbf{H}\mathbf{P}^b\mathbf{H}^{\mathrm{T}} + \mathbf{R})^{-1}, \tag{13}$$

and, in terms of the Kalman gain,

$$\mathbf{P}^a = [\mathbf{I} - \mathbf{K}\mathbf{H}]\mathbf{P}^b. \tag{14}$$

The Kalman gain [Eq. (13)] is scaled by the size of the noise process covariance ($\mathbf{R}$) relative to the $\mathbf{P}^b$ projected into observation space ($\mathbf{H}\mathbf{P}^b\mathbf{H}^{\mathrm{T}}$). The term $\mathbf{K}\mathbf{H}$ acts as a correction term to reduce $\mathbf{P}^a$ by an amount determined by the uncertainty and distribution of the observations.

Many of the following results quantify and minimize the diagonal elements of the analysis error covariance $\mathbf{P}^a$. Another metric, termed the formal mapping error ($\mathbf{E}^{\mathrm{map}}$), is the ratio of the diagonal elements of the analysis error covariance $\mathbf{P}^a$ to the background error covariance $\mathbf{P}^b$ and is a vector. The ith element of the formal mapping error $\mathbf{E}^{\mathrm{map}}$ is expressed as

$$E_i^{\mathrm{map}} = \frac{\mathbf{P}_{ii}^a}{\mathbf{P}_{ii}^b}. \tag{15}$$

Formal mapping error ($\mathbf{E}^{\mathrm{map}}$) can be used to highlight regions where observations improve the estimate and reduce $\mathbf{P}^a$.

b. Variance scaling

BGC properties have significantly different spatial and temporal variability (Fig. 3). The magnitude of the variability of these BGC signals also differs (by as much as 10 orders of magnitude, see appendix B). Without scaling, variables with

relatively large variance will dominate over variables with relatively smaller variance (see appendixes A and B). To provide equal treatment of the different properties and a reasonable representation of ocean variance, we scale the variance of individual BGC variables such that the scaled variances of all BGC variables are similar. The data scaling is a filter that imposes minimum and maximum temporal variance of each variable at each grid point.

For each variable v and depth k, we define $\text{var}_{kv}^{15\text{th}}$ to be the 15th percentile of a dataset formed by the unscaled temporal variance of the time series $\mathbf{x}(t)_{ijkv}$ at each grid point of longitude i and latitude j. Then we impose a scaling, which we call σ_{ijkv}, on the data such that

$$\text{var}_{\text{scaled}}[\mathbf{x}(t)_{ijkv}] = \frac{\text{var}[\mathbf{x}(t)_{ijkv}]}{\sigma_{ijkv}}, \qquad (16)$$

where

$$\sigma_{ijkv} = \begin{cases} \text{var}[\mathbf{x}(t)_{ijkv}], & \text{if } \text{var}[\mathbf{x}(t)_{ijkv}] \leq \text{var}_{kv}^{15\text{th}}, \\ \text{var}_{kv}^{15\text{th}}, & \text{if } \text{var}_{kv}^{15\text{th}} < \text{var}[\mathbf{x}(t)_{ijkv}] \leq 15\,\text{var}_{kv}^{15\text{th}}, \\ \dfrac{\text{var}[\mathbf{x}(t)_{ijkv}]}{15}, & \text{if } 15\,\text{var}_{kv}^{15\text{th}} < \text{var}[\mathbf{x}(t)_{ijkv}], \end{cases}$$
$$(17)$$

and where σ is the scaling term and is a function of $\text{var}[\mathbf{x}(t)_{ijkv}]$. A brief description of why the 15th percentile cutoff (and other tuning factors) were chosen can be found in appendix B. One can think of this scaling as a dynamic range limiter where small variances are amplified to the value of $\text{var}_{kv}^{15\text{th}}$ and large variances saturate and are reduced to the value of $15\,\text{var}_{kv}^{15\text{th}}$. This scaling has been tuned to reduce extremes in

CM4 output without changing the spatial distribution of BGC variance.

The sum of the variance at the ith longitude, jth latitude grid point over depth, and variable type can be written:

$$\text{var}_{i,j}^{\text{total}} = \sum_k \sum_v \text{var}_{\text{scaled}}[\mathbf{x}(t)_{ijkv}]. \qquad (18)$$

c. Localization

We expect observations at nearby grid points to be more correlated than distant observations. We hypothesize that these similarities decrease with distance and converge to a limit where grid points that are sufficiently far away are uncorrelated. However, for a variety of reasons (e.g., Cai et al. 2011), spuriously strong covariances may exist between grid points that are far apart. For this reason, imposing a filter that reduces correlations between distant points can be desirable.

Additionally, the size of the background error covariance $\mathbf{P}^b$ is $n \times n$, where n is the number of elements in the state vector $\mathbf{x}$. Necessary calculations on the $\mathbf{P}^b$ become quadratically expensive with larger n. If we expect grid points at large distances to be uncorrelated, then much of the $\mathbf{P}^b$ is close to or equal to zero; this means that much of $\mathbf{P}^b$ does not contribute to these calculations and can be ignored. Imposing a filter to remove covariances at large distances makes $\mathbf{P}^b$ a sparse matrix and substantially reduces the expense of calculations.

For these two reasons, we apply a localization filter to $\mathbf{P}^b$. The localization we use (Gaspari and Cohn 1999) is a specially constructed piecewise polynomial that does not introduce negative eigenvalues in the resulting localized matrix.

The Gaspari and Cohn localization filter contains a scaling term, s, that is defined as

$$s(r, c) = \begin{cases} -\dfrac{1}{4}\left(\dfrac{|r|}{c}\right)^5 + \dfrac{1}{2}\left(\dfrac{|r|}{c}\right)^4 + \dfrac{5}{8}\left(\dfrac{|r|}{c}\right)^3 - \dfrac{5}{3}\left(\dfrac{|r|}{c}\right)^2 + 1, & \text{if } 0 \leq |r| \leq c, \\ \dfrac{1}{12}\left(\dfrac{|x|}{c}\right)^5 - \dfrac{1}{2}\left(\dfrac{|r|}{c}\right)^4 + \dfrac{5}{8}\left(\dfrac{|r|}{c}\right)^3 + \dfrac{5}{3}\left(\dfrac{|r|}{c}\right)^2 - 5\left(\dfrac{|r|}{c}\right) + 4 - \dfrac{2}{3}\left(\dfrac{c}{|r|}\right), & \text{if } c \leq |r| \leq 2c, \\ 0, & \text{if } 2c \leq r, \end{cases}$$
$$(19)$$

where $|r|$ is the magnitude of the distance between grid points, and c is the characteristic length scale of the localization. The localization is applied elementwise such that the resulting covariance matrix is calculated as

$$\mathbf{P}^b = \begin{bmatrix} p_{11}s(0, c) & p_{12}s(r_{12}, c) & \cdots & p_{1K}s(r_{1K}, c) \\ p_{21}s(r_{21}, c) & p_{22}s(0, c) & & \\ \vdots & & \ddots & \\ p_{K1}s(r_{K1}, c) & & & p_{KK}s(0, c) \end{bmatrix}, \qquad (20)$$

where $p_{a,b}$ is the covariance between the ath and bth elements of the state vector $\mathbf{x}$, and r_{ab} is the horizontal distance between the ath and bth element of the state vector.

Ideally, the characteristic length scale c will be proportional to the length scale of the forcing that produces the covariance. We observe that the gravest eigenvectors of the covariance matrix (Figs. 4 and 5) correspond to either large-scale seasonal oscillations or waves, and higher eigenmodes of the covariance matrix (Fig. 4) appear to demonstrate finer mesoscale variability. For this reason, we impose a scale separation on the 4 gravest eigenmodes of the covariance matrix. The localization applied to the gravest eigenmodes had a c value of 10.95° latitude and longitude, while localization applied to all higher modes had a c value of 3.65° latitude and longitude. The localized covariances are represented as the blue square labeled $\mathbf{P}^b$ in Fig. 7.

d. Variance constrained by static Argo arrays

Now that we have scaled and localized $\mathbf{P}^b$, we focus on describing the calculation of the first of our three results: variance constrained by static distributions of Argo floats. We produce two results from the static arrays: variance constrained from an actual array of Argo floats at an example time, May 2021, which we term the "existing float array snapshot," and variance constrained from randomly deployed floats, which we term the "Monte Carlo snapshot" (Fig. 1). Equations (13) and (14) are used to calculate $\mathbf{P}^a$. This section describes the construction of the observation operator $\mathbf{H}$ (Argo array) and the noise process covariance $\mathbf{R}$ (estimate of observational error), which are the two required matrices to calculate $\mathbf{P}^a$.

We will describe the construction of these matrices for the general float array and then explain the specifics of the existing float array snapshot and Monte Carlo snapshot. The observation operator accounts for every float's observational suite. Because $\mathbf{x}$ includes multiple BGC variables at a grid cell, an individual Argo float profile must be considered as multiple distinct observations. The float array is binned to match the dimensions of the state vector $\mathbf{x}$. Multiple floats can occupy the same grid cell: for example, a core Argo and BGC Argo float could be separated by approximately two hundred kilometers for $2° \times 2°$ grid spacing and farther for coarser resolutions. Let the list O of length m be the unique state vector index corresponding to the distribution of sensors on floats in the array. To account for the additional variance constrained by redundant sensors in a grid cell, we also record the number of measurements per element of $\mathbf{x}$ and call this list N. List N is also of length m. From the fundamental observation equation [Eq. (1)], we see that the observation operator $\mathbf{H}$ is an $m \times n$ matrix, where n is the length of the state vector. The observation operator projects the state vector into the observation space in the observation equation. The observation operator is a sparse matrix composed of ones at the column indices defined in list O and zeros elsewhere. This can be written as the following:

$$\mathbf{H}[1, O_1] = 1$$
$$\mathbf{H}[2, O_2] = 1$$
$$\vdots$$
$$\mathbf{H}[m, O_m] = 1. \qquad (21)$$

To calculate $\mathbf{R}$ in Eq. (13) we assume that the representation error of ϵ [Eq. (1)] dominates the instrumentation error and is proportional to the uncertainty variance of the state vector for the observation location and variable type. We also assume that additional observations at a grid point reduce the representation error. $\mathbf{R}$ is a diagonal $m \times m$ matrix with diagonal elements equal to 4 times the variance of the state vector element corresponding to the observation scaled by the number of observations. This approximation is a conservative choice because one observation every 10 days can only constrain a limited percentage of the total variance. In matrix form, this is written as

$$\mathbf{R} = 4 \begin{bmatrix} \mathbf{P}(O_1, O_1)/N_1 & 0 & \cdots & 0 \\ 0 & \mathbf{P}(O_2, O_2)/N_2 & & \\ \vdots & & \ddots & \\ 0 & & & \mathbf{P}(O_m, O_m)/N_m \end{bmatrix}. \qquad (22)$$

Given the array distribution of the existing Argo floats (Fig. 1), it is straightforward to calculate the $\mathbf{H}$ and $\mathbf{R}$ matrices that correspond to the existing float array snapshot. The analysis error covariance, $\mathbf{P}^a$ [Eq. (14)], and formal mapping error $\mathbf{E}^{map}$ [Eq. (15)], were then calculated for all depth levels. Schematically, this is represented in Fig. 7 as the combination of the observation operator $\mathbf{H}$ (existing float array) and background error covariance $\mathbf{P}^b$ (modeled cross covariances) to produce the present $\mathbf{P}^a$.

Uniform float distribution has been a stated design goal of the core Argo array and is a design goal of the BGC Argo array (Johnson and Claustre 2016). We examine whether nonuniform distribution might be more efficient, that is, reduce the numbers of floats required, by first estimating the amount of variance the uniformly distributed BGC Argo array will constrain by creating Monte Carlo snapshots of many randomly distributed arrays of varying float densities and averaging the results together. Random arrays were constructed of hypothetical floats equipped with the full CM4 BGC sensor suite, and array sizes were calculated from 0 to 1000 floats in 50 float increments. We calculated Monte Carlo variance snapshots for 50 random arrays at each array size and averaged the results. Schematically, this is represented in Fig. 7 as the combination of the random float array and cross covariances to produce the designed $\mathbf{P}^a$.

e. The transition matrix and variance constrained by future Argo arrays

Now that we have a quantifiable metric for assessing float performance for constraining the temporal variability of a state vector, we consider the task of predicting future float distributions so that we can estimate how well the Argo array will observe the ocean at a future time. For these calculations, we assume that the statistics of the background error covariance $\mathbf{P}^b$ are stationary. A $2° \times 2°$ spatially binned transition matrix with a 90-day time step, constructed from all existing Argo trajectories (Chamberlain et al. 2023) (Fig. 6), is used to estimate the evolving array distribution at later time steps. The transition matrix acts on the Argo state vector ($\boldsymbol{\rho}$), which is defined as the probability of finding an Argo float in each grid cell, and propagates it into the future l time steps such that

$$\boldsymbol{\rho}(t + l) = \mathbf{M}^l \boldsymbol{\rho}(t), \qquad (23)$$

where $\mathbf{M}$ is the transition matrix. The vector $\boldsymbol{\rho}$ is $n \times 1$, where the superscript tm indicates transition matrix. The transition matrix is a square $n \times n$ matrix that statistically predicts the future probability density of the Argo state vector as it evolves through time. Transition matrix coverage is restricted to regions with a large amount of Argo trajectory data; therefore, while the transition matrix is on the same grid as CM4, the transition matrix grid is a subset of the CM4 grid.
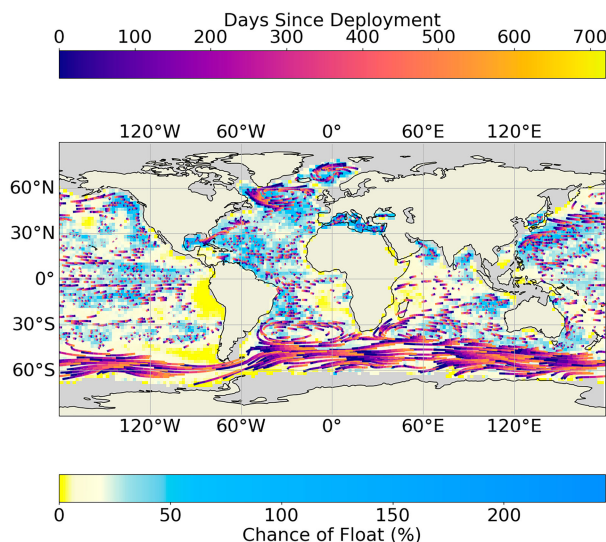
FIG. 6. The 2-yr prediction of array density of global core Argo array. Argo array distribution is based on the May 2021 snapshot (Argo 2021) using the transition matrix (Chamberlain et al. 2023) [Eq. (23)]. Colored lines represent time of mean transition [l in Eq. (24)]. Gridcell shading represents estimated array density. Gray shading represents areas outside domain of the transition matrix; beige shading represents land.

The first statistical moment of the transition matrix can be expressed as

$$\mathbf{r}_a = \sum_{b=1}^{n^{\text{tm}}} \mathbf{M}_{ab}^l \mathbf{r}_b, \tag{24}$$

where $\mathbf{r}_b$ is the relative displacement vector from grid cell a to grid cell b, and $\mathbf{M}_{ab}^l$ is the probability of transition from grid cell a to grid cell b. This first moment of the transition matrix probability distribution can be interpreted as the expected value of the transition. Using this equation, we can estimate the future location of an Argo float to any time step in the future. An example of the deployed Argo fleet from the May 2021 snapshot projected from 90 days to 4 years in the future is seen as the colored curves in Fig. 6.

The approximate lifespan of full float functionality is approximately 5 years. In our estimates of the future float distributions, we account for float age by removing floats from the distribution that are over 5 years old. For these examples, we do not include the ongoing replacements that maintain the global array at about 4000 floats.

Figure 7 represents the future float PDF as the existing float array operated on by the transition matrix; the future float PDF is combined with the background error covariance $\mathbf{P}^b$ of CM4 to produce an estimate for future analysis error covariance $\mathbf{P}^b$.

f. Optimal array design

An optimal array utilizes the observations of every float to the greatest effect. The criteria defined as optimal in this approach are to minimize the expected error variance for the estimated anomaly of multiple BGC properties from the surface to 2000 m depth. Our strategy to determine optimum deployment locations is iterative: placing floats in an ideal location one at a time. This means that every time a new float is added to the system, we must find the next best location to deploy a float or, stated another way, the deployment location that constrains the most variance in the analysis error covariance $\mathbf{P}^a$. Naively, one might assume that deploying in the localized $\mathbf{P}^a$ grid cell of most variance is the best choice. However, this does not consider the spatial covariance or cross covariances of observations. An observation at one grid cell can constrain variance of the same or different variables many grid cells
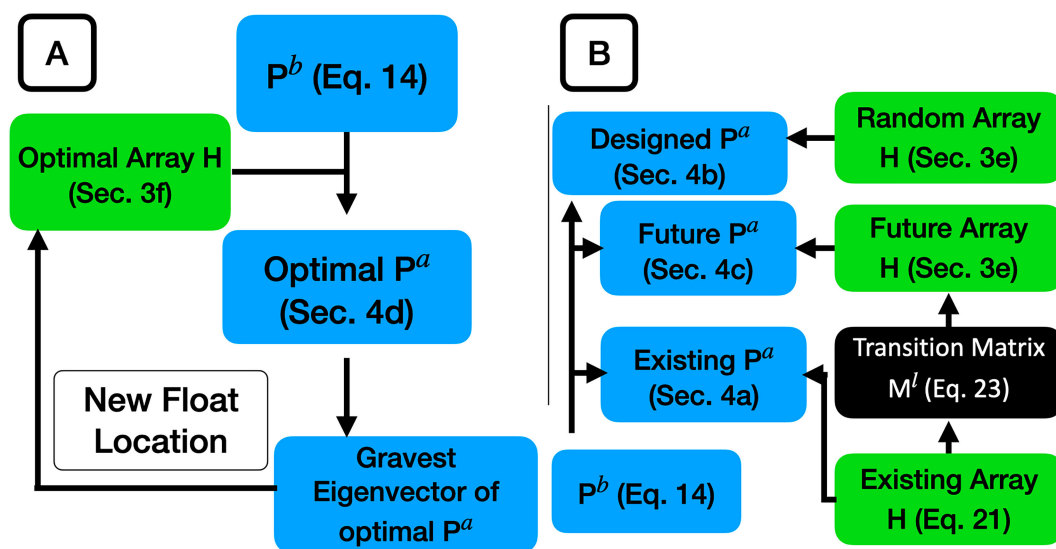

FIG. 7. (a) Flowchart of optimal deployment location calculation and (b) organization of analysis error covariance $\mathbf{P}^a$ products.
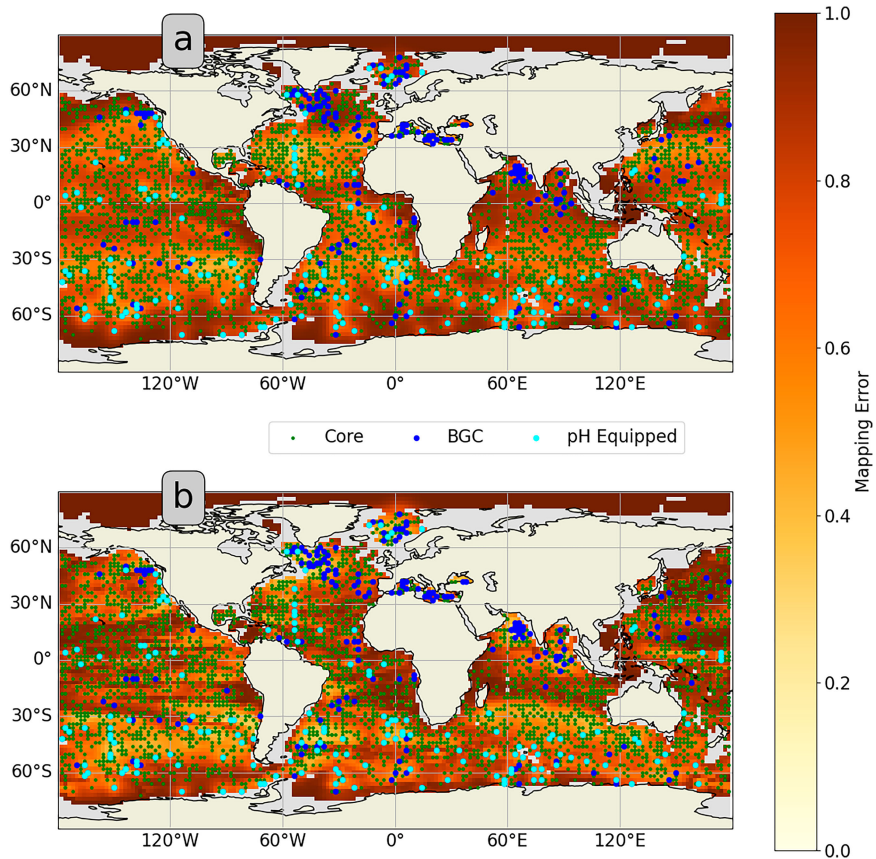
FIG. 8. Scaled pH formal mapping error ($\mathbf{E}^{\text{map}}$) of existing core and BGC Argo float array taken from May 2021 snapshot at (a) the surface and (b) 1000 m. Colored shading represents amount of unconstrained variance. Beige shading represents land. Gray areas are too shallow. Green dots represent core Argo floats. Blue dots represent BGC Argo floats without pH sensors. Cyan dots represent BGC floats equipped with pH sensors.

away. The structure of $\mathbf{P}^a$ can be complicated and difficult to understand. The gravest eigenvector of $\mathbf{P}^a$ will always contain the most variability in the eigenspectrum, and we assume the next best location is the maximum absolute value of this gravest eigenvector.

The iterative strategy is illustrated in Fig. 7a. Starting with an observation operator $\mathbf{H}$ [Eq. (14)], which is formed from a distribution of floats ($\mathbf{H}$ can be the null matrix if there are no floats), we calculate $\mathbf{P}^a$ ($\mathbf{P}^a$ will be $\mathbf{P}^b$ if this is the first float in the array). Next, we calculate the gravest eigenvector of $\mathbf{P}^a$ and find the location of the maximum sum of absolute value of the eigenvector weights [similar to Eq. (18)]. Finally, we add a float in the optimal array at this location and recalculate $\mathbf{P}^a$. Floats are iteratively added until the maximum number of floats in the simulation has been reached.

In previous results, we calculated $\mathbf{P}^a$ and $\mathbf{E}^{\text{map}}$ on a single depth level. However, a single depth state vector would not be appropriate for this optimization because the ocean experiences different forcing and has different variability at different depths. An optimized observing strategy needs to be representative of the diverse range of physical and biogeochemical processes that occur at different depths in the ocean;

but, as noted previously, increasing the size of the state vector is computationally expensive, and so a balance must be struck between the two. The state vector $\mathbf{x}$ used in these calculations includes BGC variables from CM4 at depths 15, 87.5, 550, and 950 m subsampled to a 4° × 4° grid of latitude and longitude. This method weights all variables, at all depths, equally. Equal weighting might not be the correct choice for all applications, as some variables (such as those related to the carbon cycle) may have more scientific or societal relevance. Adjusting weights to the relative importance of these observations can easily be done by adjusting σ in Eq. (17); however, it is outside the scope of this work to recommend alternate weightings.

4. Results

a. Estimates of variance constrained by the current Argo float array

The ability of the combined core and BGC Argo float arrays from the May 2021 snapshot (Argo 2021) to observe the BGC anomaly from the mean is quantified. Argo locations are used to create an observation operator [$\mathbf{H}$ in Eq. (21)].
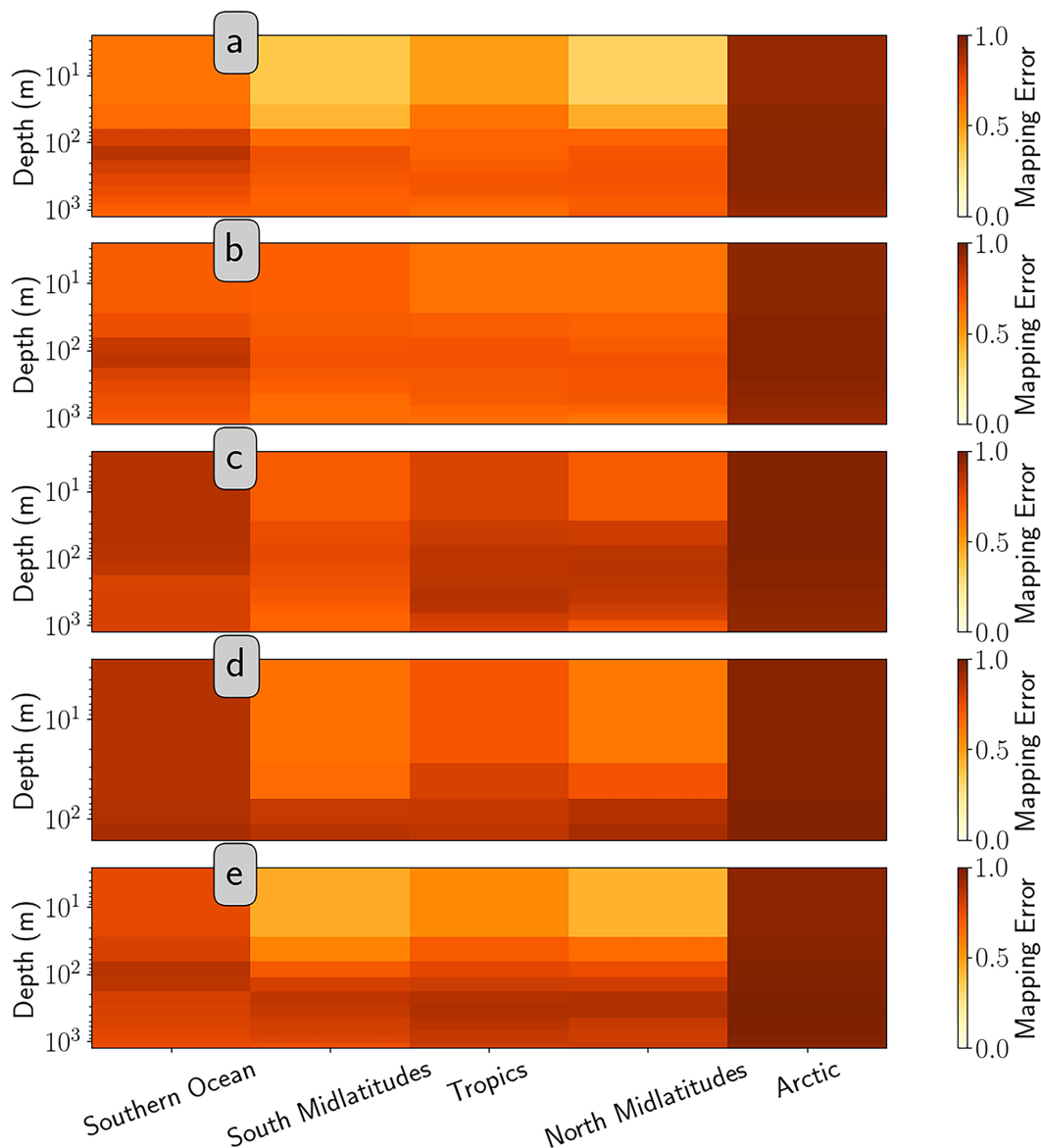
FIG. 9. Zonal average formal mapping error ($\mathbf{E}^{\mathrm{map}}$) of existing Argo core and BGC float array at all depths of (a) temperature, (b) salinity, (c) pH, (d) chlorophyll, and (e) oxygen. (Zones are defined as follows: Southern Ocean: south of 60°S; southern midlatitudes: 60°–20°S; tropics: 20°S–20°N; northern midlatitudes: 20°–60°Nl; Arctic: north of 60°N.)

This $\mathbf{H}$ is then used to calculate the $\mathbf{P}^a$ [Eq. (14)]. Figure 8 is an example of the formal mapping error $\mathbf{E}^{\mathrm{map}}$ [Eq. (15)] of pH for the current Argo array. $\mathbf{E}^{\mathrm{map}}$ depends on the correlation scales for the variables considered. Generally, $\mathbf{E}^{\mathrm{map}}$ is larger at depth because spatial correlation scales are shorter (although temporal correlation scales may be longer) (Fig. 9). The largest $\mathbf{E}^{\mathrm{map}}$ occurs in the Arctic, where there are very few floats. The high-latitude Southern Ocean is the region with the next largest mapping error, followed by the tropics. The value of $\mathbf{E}^{\mathrm{map}}$ is smallest in the northern and southern midlatitude surface waters. These regions tend to have very long spatial correlation scales. Figure 10 shows the zonal

average of unconstrained variance for all variables based on the current Argo array.

Rather than minimizing formal mapping error $\mathbf{E}^{\mathrm{map}}$ [Eq. (15) and Fig. 9], we could choose to minimize analysis error covariance $\mathbf{P}^a$ (Fig. 10). $\mathbf{E}^{\mathrm{map}}$ represents how well a region is observed, but even well-observed regions with high variance can have relatively high $\mathbf{P}^a$; an example of this is seen in surface temperature in the northern midlatitudes (Fig. 10a). The Arctic shows high $\mathbf{P}^a$ in surface salinity and chlorophyll. As the Arctic is almost entirely unobserved by Argo, this means that Arctic variability of analysis error covariance $\mathbf{P}^a$ and background error covariance $\mathbf{P}^b$ are similar. Maximum pH and oxygen $\mathbf{P}^a$ are observed in the
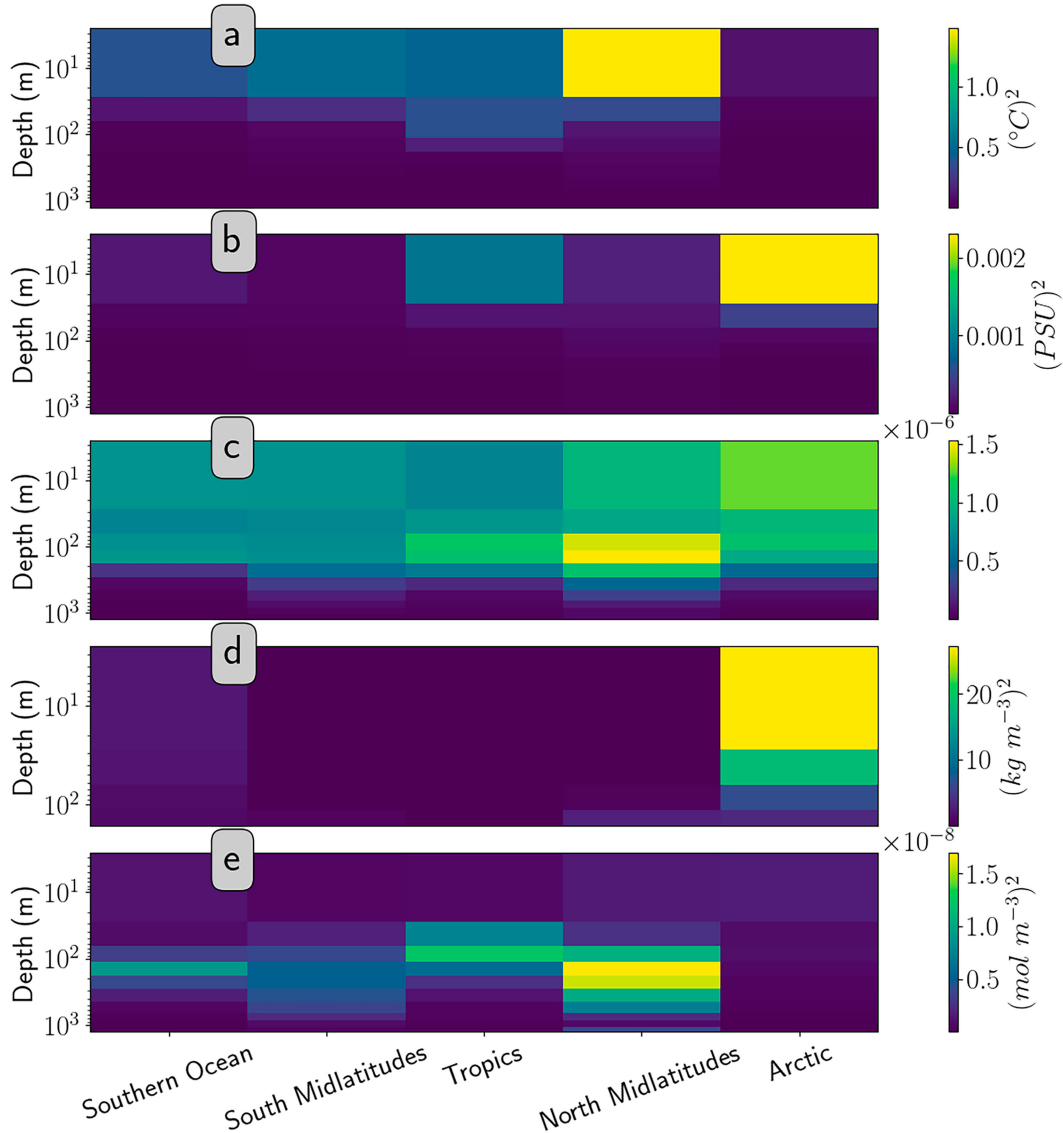
FIG. 10. Zonal average analysis error covariance $\mathbf{P}^a$ of existing Argo core and BGC float array at all depths, of (a) temperature, (b) salinity, (c) pH, (d) chlorophyll, and (e) oxygen. (Zones are defined as follows: Southern Ocean: south of 60°S; southern midlatitudes: 60°–20°S; tropics: 20°S–20°N; northern midlatitudes: 20°–60°N; Arctic: north of 60°N.)

subsurface at northern midlatitudes. The Southern Ocean and Southern Hemisphere midlatitudes have relatively low $\mathbf{E}^{\mathrm{map}}$ and $\mathbf{P}^a$. This is due to the impact of the SOCCOM project, which has deployed a substantial number of BGC floats in these regions.

b. Estimates of variance constrained by Monte Carlo distributions

Estimates for variance constrained by varying numbers of randomly deployed BGC Argo arrays of varying uniform densities have been calculated (Fig. 11). Random distributions of floats were used to create observation operators [$\mathbf{H}$ in Eq. (21)], which were used to calculate the analysis error

covariance $\mathbf{P}^a$ [Eq. (14)]. Fifty Monte Carlo snapshots were calculated for each float density considered, and the results were averaged.

As expected, $\mathbf{P}^a$ is inversely proportional to float density for the 5 variables considered. Maximum $\mathbf{P}^a$ in temperature, salinity, and chlorophyll occurs in the surface layers, where pH and oxygen have high uncertainty at 100 m, and oxygen has maximum uncertainty at depth (Fig. 11). High oxygen $\mathbf{P}^a$ at depth is due to large unobserved variance in the Sea of Japan. This area is known for bottom water formation (Talley et al. 2003).

The decrease in formal mapping error ($\mathbf{E}^{\mathrm{map}}$) is not uniform across variables and depths. Salinity and oxygen have
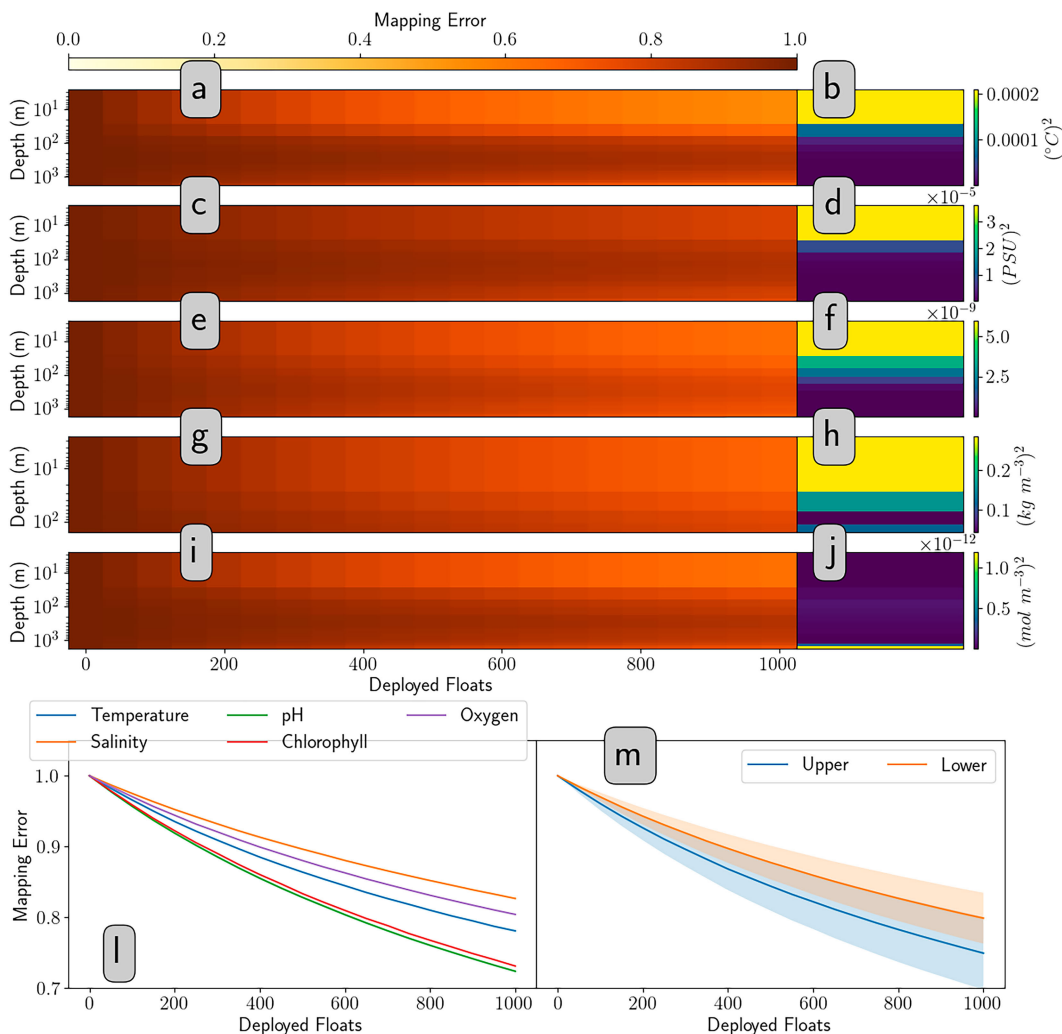
FIG. 11. (a)–(j) Global average of formal mapping error ($\mathbf{E}^{\mathrm{map}}$) of (left) randomly distributed Argo floats for increasing float density and (right) analysis error covariance $\mathbf{P}^a$ for 1000 BGC floats at all depths of (a),(b) temperature, (c),(d) salinity, (d),(e) pH, (e),(f) chlorophyll, and (f),(j) oxygen. (l) Colored lines represent depth averaged $\mathbf{E}^{\mathrm{map}}$ by variable for increasing Argo float density. (m) Colored lines represent variable averaged $\mathbf{E}^{\mathrm{map}}$ for upper and lower ocean depths. Upper ocean is defined as shallower than 137.5 m, and deep is defined as deeper than 137.5 m. Shading represents standard deviation across all variables.

the slowest decrease in $\mathbf{E}^{\mathrm{map}}$ with increasing number of floats (hardest signals to constrain), and pH and chlorophyll have the steepest decrease in $\mathbf{E}^{\mathrm{map}}$ with increasing number of floats (easiest to constrain). The covariance of pH with temperature and oxygen has substantial covariance, and the $\mathbf{E}^{\mathrm{map}}$ of pH decreases an average of 12% faster than the mapping error of salinity with increasing number of floats. This work suggests that additional core Argo floats may need to be augmented with oxygen sensors in order to achieve a mapping error equivalent to that of pH.

When binned by depth, upper-ocean formal mapping error ($\mathbf{E}^{\mathrm{map}}$), averaged across variables and by depth, had a steeper decline than the deep ocean with increasing floats; overall upper-ocean $\mathbf{E}^{\mathrm{map}}$ decreased an average of 6% faster. The upper ocean is defined as everything shallower than

137.5 m and the deep ocean is defined as everything deeper than 137.5 m.

c. Estimates of variance constrained by future Argo floats

The ability of time-evolving Argo float arrays to observe BGC variance is quantified here for the first time. These maps can identify future holes in the BGC Argo array or be used to justify the continued investment in these observations. The future analysis error covariance $\mathbf{P}^a$ was calculated by propagating the current float distribution into the future with the Argo trajectory-based transition matrix [Eq. (23)]. The first moment of the transition matrix [Eq. (24)] was used to determine future float locations and construct a future observation operator [$\mathbf{H}$ in Eq. (21)]. The future observation operator was then used to estimate $\mathbf{P}^a$ [Eq. (14)].
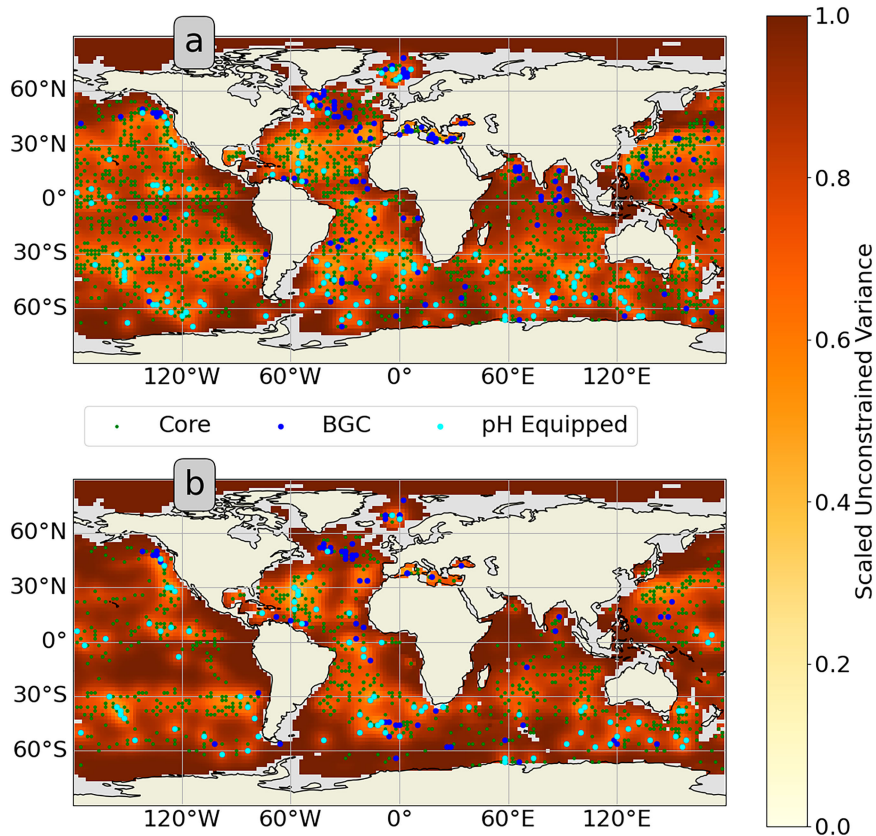
FIG. 12. Scaled surface pH formal mapping error ($\mathbf{E}^{\text{map}}$) of the Argo float array of May 2021, projected at (a) 1 and (b) 2 years into the future assuming floats are not replenished. Colored shading represents amount of $\mathbf{E}^{\text{map}}$. Beige shading represents land. Gray areas are too shallow to be calculated in simulations. Green dots represent locations of existing core Argo floats. Blue dots represent locations of existing BGC Argo floats. Cyan dots represent floats equipped with pH sensors.

Similar to section 4b, the unconstrained BGC variance is inversely proportional to the array size. As the array is projected into the future, without replenishment, such that an increasing number of floats are removed due to age, the variance increases. Also, the distribution of highest variance is similar to the results shown in section 4b: namely, high unconstrained surface variability in temperature, salinity, and chlorophyll, and high unconstrained 100 m variability in pH and oxygen (Figs. 12 and 13).

To highlight the utility of this method, we deployed 2 hypothetical BGC Argo floats at the start (float 1) and end (float 2) of the GO-SHIP P1 transect that sailed in fall 2021 (Fig. 14). Our method calculated the relative performance of these two hypothetical floats within the context of the natural BGC variability of the ocean (as realized by CM4) and within the context of the surrounding float array from the May 2021 Argo snapshot. The transition matrix evolved the position (and accompanying algorithm-estimated death) of these and surrounding floats forward through time. The value of $\mathbf{P}^a$ was calculated for each float deployment, and their difference in analysis error covariance $\mathbf{P}^a$ quantified their relative performance

at each time step. This calculation was done for all BGC variables in this study, from CM4. Float 1 convincingly outperforms float 2 in pH variance constrained in the entire water column and temperature variance constrained at depth throughout the experiment. In contrast, float 2 constrains more salinity and oxygen variance throughout the experiment. Changes in which float constrains more variance also occur through time, particularly in chlorophyll at 200 m and salinity at the surface and 600 m. Argo managers are ultimately responsible for maximizing the relative value of observations collected by floats, and this is a first step at quantifying the relative importance of potential deployment sites with respect to the assumption here of observing the anomaly from the mean.

d. Optimal array design

An optimal array based on BGC floats has been constructed to best constrain global BGC variability (Fig. 15). The method to calculate the optimal array takes an iterative approach by sequentially finding the next best float deployment. The best deployment location is approximated as the
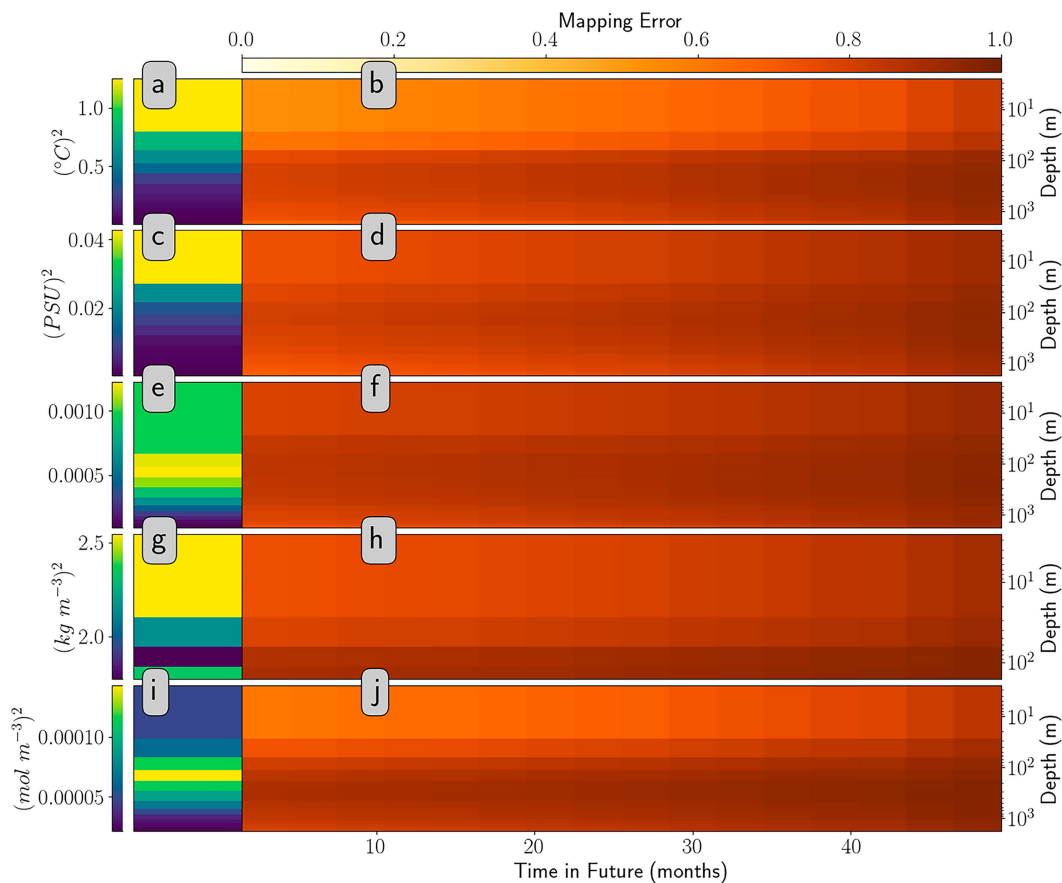
FIG. 13. Global average of the covariance of (left) the analysis error covariance $\mathbf{P}^a$ of the existing core and BGC Argo float array and (right) formal mapping error ($\mathbf{E}^{\mathrm{map}}$) of the predicted Argo array at all depths: (a),(b) temperature, (c),(d) salinity, (e),(f) pH, (g),(h) chlorophyll, and (i),(j) oxygen.

maximum absolute value of the sum of variances [Eq. (18)] of the gravest eigenvector of the analysis error covariance $\mathbf{P}^a$ [Eq. (14)]. The new deployment location is then added to the observation operator $\mathbf{H}$ [Eq. (21)], and a new $\mathbf{P}^a$ is calculated. This iterative method is run until the entire array is constructed (Fig. 7).

The optimal float array was calculated for 1000 floats, which is the specification for the BGC Argo array (Johnson and Claustre 2016), and achieved global coverage (Fig. 15a). The meridionally binned optimal array (Fig. 15c) does not have a prominent structure; however, the zonally binned optimal array (Fig. 15b) has five distinct peaks in the distribution: two large peaks in the subtropical gyres around 45°N and S, two smaller peaks in the Arctic and in the equatorial region, and a narrow peak in the high-latitude Southern Ocean. The algorithm does not favor deployments in the boundaries that exist between the subtropical gyres, the equatorial region, the Arctic, or in the Antarctic Circumpolar Current. We hypothesize this is due to strong dynamical variability in these regions leading to shorter correlation length scales and smaller cross covariances. The algorithm also does not favor BGC Argo deployments in the western

tropical Pacific. This is apparently because there is lower BGC variance in CM4 in this region (see appendix A) and is considered in section 5b.

The efficacy of the optimal array was tested in two ways. First, to test the distribution of variability in CM4, random and optimal arrays were used to constrain uncertainty covariance matrices degraded with Gaussian noise. Second, the optimal array was compared to random arrays of varying number of floats (Fig. 16). In the first test, we added Gaussian noise with a scaling equal to that of the localization to the background error covariance $\mathbf{P}^b$ and calculated the amount of unconstrained variance (diagonal of $\mathbf{P}^a$) for both 1000 float random arrays and the 1000 float optimal array. The amount of noise added was scaled to be proportional to the variance at each grid point with signal-to-noise ratios (SNR) ranging from 10^3 to 10^{-2}. To develop adequate sensitivity statistics, these calculations were repeated with unique Gaussian noise and random float arrays 50 times at every SNR. Figure 16 shows that the optimal array outperformed the random arrays at all levels of SNR, although the relative outperformance decreased by half in the noisier cases.
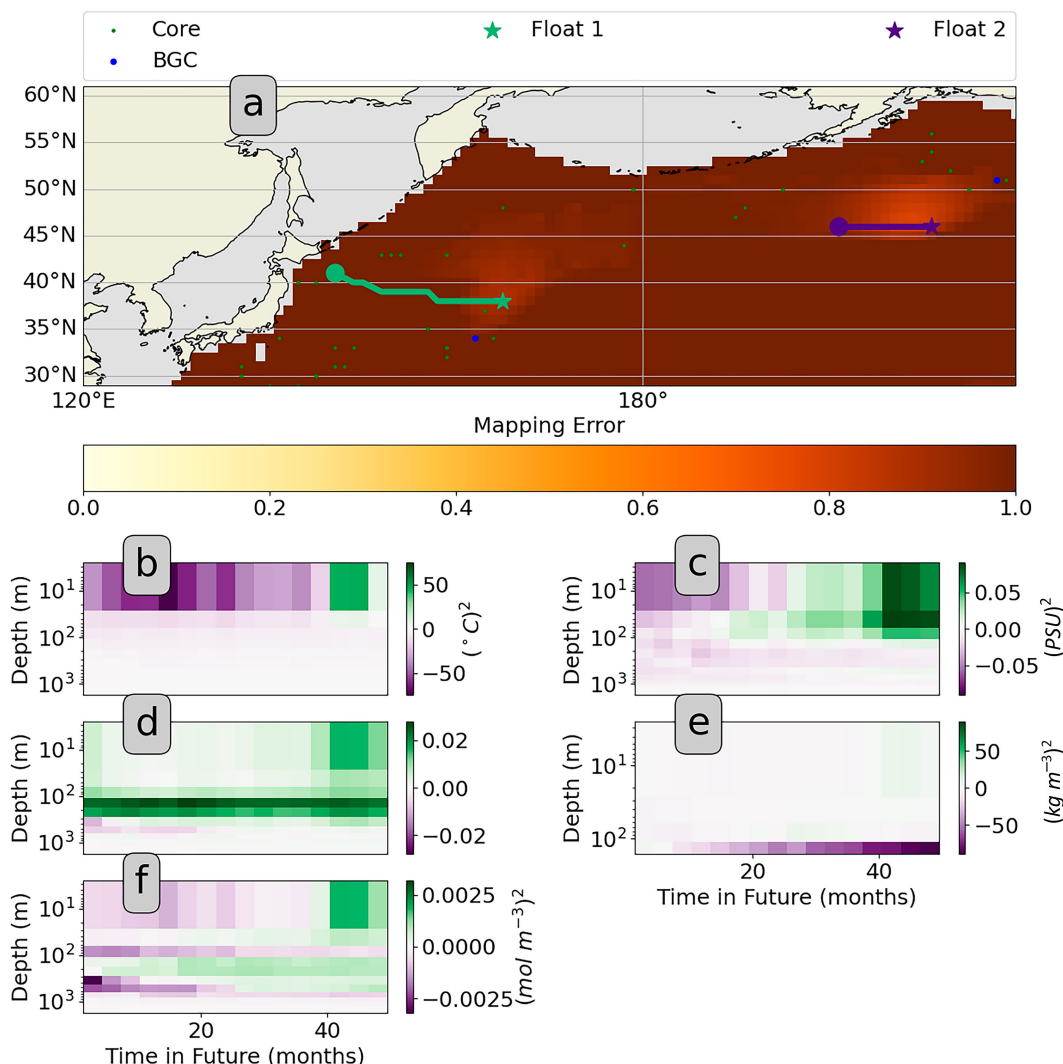
FIG. 14. (a) Formal mapping error ($\mathbf{E}^{\mathrm{map}}$) and track lines of two hypothetical floats deployed along the P1 GO-SHIP line 48 months after deployment with surrounding Argo infrastructure as represented by the May 2021 snapshot. All Argo floats (hypothetical and real) are propagated to future positions with the transition matrix. Green dots represent core Argo floats, and blue dots represent BGC Argo floats. Teal and purple circles represent deployment locations, teal and purple lines are track lines, and teal and purple stars represent final locations of float 1 and float 2, respectively. Gray shading indicates the region outside of the model domain. Beige shading indicates land, and colored shading indicates mapping error. (b)–(f) Difference of float 1 and float 2 expected error variance for (b) temperature, (c) salinity, (d) pH, (e) chlorophyll, and (f) oxygen. Green shading indicates float 1 constrains more variance and purple shading indicates float 2 constrains more variance.

The second test was designed to test the efficacy of the optimal array. The unconstrained variance (diagonal of $\mathbf{P}^a$) was calculated for both the optimal and random arrays with an increasing number of floats. Again, these calculations were repeated with 50 unique random float distributions for each random float density. The 1000-float optimal array constrained an equivalent amount of variance as the mean 1100-float random array (Fig. 16). Of course, this idealized experiment does not take into account the reality that floats are mostly deployed from research ships of opportunity rather than along the most optimal tracks. This experiment does,

however, offer insight into regional prioritization of BGC deployments.

5. Discussion

a. Expected error variance structure

We have demonstrated a method to estimate the impact of present and future BGC Argo arrays on constraining variance in the float-observed BGC fields. The results show consistent structures in the analysis error covariance $\mathbf{P}^a$ seen in the current, future (projected), and uniformly distributed arrays. The
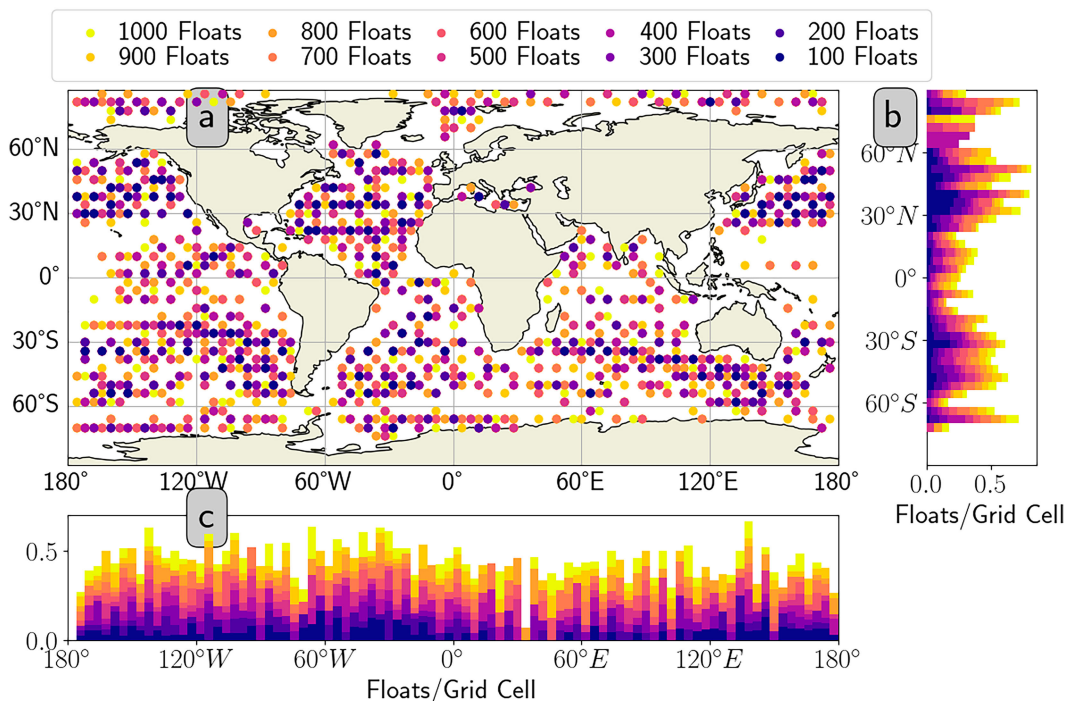
FIG. 15. (a) Map of the optimal distribution of 1000 BGC Argo floats with a grid spacing of approximately 6° in latitude and longitude. Dots represent ideal BGC Argo float locations for observing the BGC anomalies from the mean. State vector used for calculation is based on four depth levels (15, 87.5, 550, and 950 m) of CM4 BGC output at a grid spacing of 4° in latitude and longitude. Beige shading indicates land. (b) Histogram of zonally binned optimal array. (c) Histogram of meridionally binned optimal array. The histograms in (b) and (c) are binned in increments of 6° latitude and longitude, respectively. Colored shading indicates when in the sequential calculation floats were deployed (i.e., purple indicates locations identified first, and yellow indicates locations identified last). Float locations identified earlier are relatively more important in this optimal configuration by construction.

consistent structure of $\mathbf{P}^a$ among these 3 distributions is not surprising because the design criteria for the current Argo fleet is a uniform distribution, so these reflect the same sampling strategy. We observe that the general structure of the $\mathbf{P}^a$ matches the structure of the background error covariance $\mathbf{P}^b$: higher temperature variability in the Northern Hemisphere midlatitudes, higher salinity and chlorophyll variability in the Arctic, and higher pH and oxygen variability in the Northern Hemisphere midlatitudes at a depth of 100 m (see appendix C).

The $\mathbf{P}^a$ estimate presented only considered Argo floats. Additional observing platforms such as buoys, gliders, and satellites, constrain additional variance that has not been accounted for here. The largest moored buoy arrays (TAO, RAMA, and PIRATA) are located in the tropics and record high-frequency full-depth observations of temperature, salinity, and limited BGC variables. These observations constrain ocean variance in these regions, and the unconstrained variance in the tropics is undoubtedly lower than shown in these results. Additionally, satellite observations measure important ocean variables such as temperature, salinity, sea surface height, and chlorophyll; consequently, the unconstrained variance in the surface ocean of BGC variables is lower than presented here.

The BGC variance estimates presented are operationally idealized and ignore ice or the difficulty of deploying floats in remote regions. Some of this ocean variability may be unobservable in the real world with Argo floats. While the seasonal extent of the Southern Ocean sea ice cover offers many opportunities for floats to surface during the austral summer, a substantial area in the Arctic is continuously covered. Also, conventional Argo float ballasting is unsuitable for the Arctic, and new float designs with reserve buoyancy will be necessary. This challenge is being overcome by recently funded proposals to deploy acoustically tracked under-ice floats in the Arctic, but Arctic observations will always be comparatively difficult. The optimal maps described here are agnostic to the platform used to collect the observations, and, given the grave importance of Arctic monitoring, a combined observing strategy of gliders, floats, and ships may be necessary.

In this analysis, we have only considered the spatial correlation of observations. However, for applications such as data assimilating models, quantifying the spatiotemporal impact of observations may be a better metric of observing design. At the surface, high temporal variability of surface fluxes is not captured in 10-day sampling, and a larger observational uncertainty may be needed to realistically map these fields. At
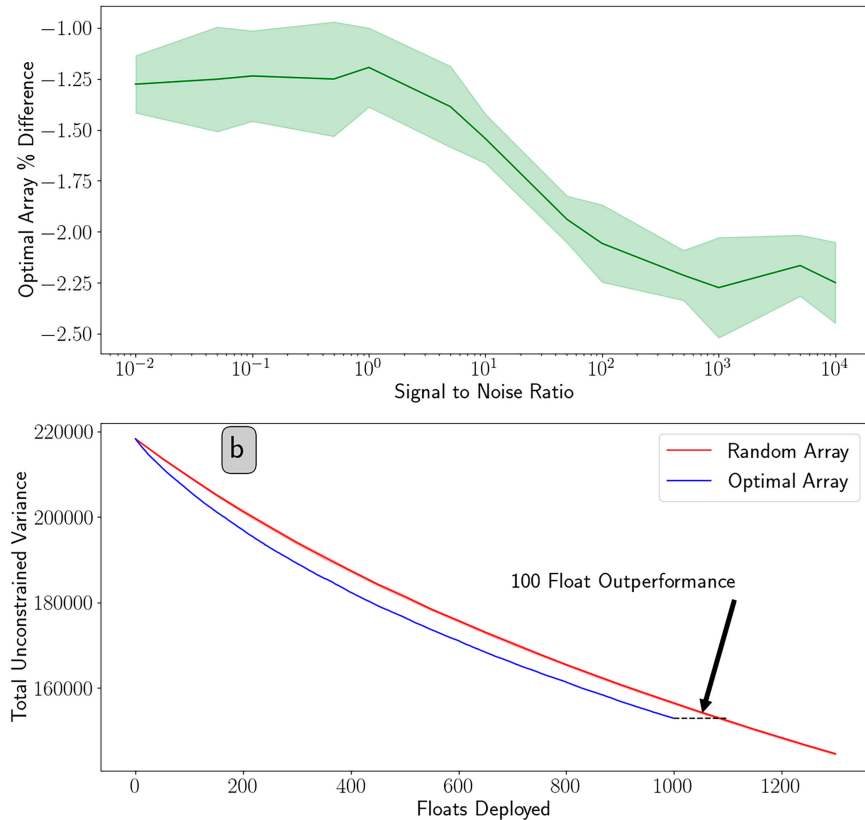
FIG. 16. (a) Relative unconstrained variance—sum of diagonal of the analysis error covariance $\mathbf{P}^a$—of randomly distributed 1000 float arrays and the optimal 1000 float array with Gaussian noise added to the background error covariance $\mathbf{P}^b$ at varying signal-to-noise ratios (SNRs). Calculations were repeated 50 times at each SNR. Green line represents mean of ensemble of calculations, and green shading represents standard deviation of ensemble of calculations. (b) Total unconstrained variance—sum of diagonal of $\mathbf{P}^b$—of randomly distributed (red line) and optimal (blue line) float arrays of increasing distributions. Blue line represents variance constrained by the optimal array, and red line represents mean of variance constrained by random array. Black dash indicates the difference in array density of the random float array necessary to achieve an equivalent constrained variance of the optimal float array at 1000 floats.

depth, forcing happens on much slower time scales (weeks to months), and information about the state of the deep ocean may persist in the system longer than individual profiles. This means that the observations of multiple profiles could be combined into the same mapped product, similar to the widely used climatologies of Roemmich and Gilson (2009) or data assimilating models (Mazloff et al. 2010). The temporal autocovariance of the state could be quantified in $\mathbf{P}^a$, but this would be substantially more computationally expensive.

b. Optimal array recommendations

The method (section 3f) for determining the optimal array calculates the next best float deployment location for observing the anomaly from the mean. This method assumes the mean of BGC fields is already known. The algorithm prioritizes deployment of the first floats in the northern midlatitudes centered at 40°N and in the southern midlatitudes centered at 45°S. From this analysis, a large initial investment

in Southern Ocean BGC deployments through the SOCCOM project was a wise first choice. Building on SOCCOM, the next latitude band this method recommends is centered at 45°N, then the Arctic (if possible), followed by the equatorial region. These results also define which areas should be prioritized for replenishment. With a finite number of BGC floats each year and ships of opportunity to deploy from, the north and south midlatitudes are prioritized over the tropics.

The southern midlatitudes are noted as a region of spuriously high ventilation and consequently biased biogeochemistry in the CM4 model (Dunne et al. 2020), which likely results in unrealistic biogeochemical covariances. Because of this, one might expect to see an anomalously high density of floats in southern midlatitudes, but the distribution of floats in the northern and southern midlatitudes is relatively even. The relative unimportance of the tropics to BGC variability as calculated from this method (section 3f) is not uniform and is concentrated in the western Pacific. In the depths considered,

this region has the lowest combined scaled variance [Eq. (18)] (see appendix A). The *World Ocean Atlas* climatology also shows the western Pacific as a region of distinctly low spatial variability for the depths and variables considered (Locarnini et al. 2018; Zweng et al. 2019; Garcia et al. 2019b,a), which lends support to this result. However, the low temporal variability in the western Pacific may result from the spatially restrictive localization used to construct the background error covariance $\mathbf{P}^b$; the western tropical Pacific is a region that participates in powerful, large-scale teleconnections via the shape and extent of western boundary currents, the phase of Madden–Julian oscillations, and the ENSO cycle. The western equatorial Pacific results here highlight how array optimization methodologies can lead to different array distribution recommendations and are, in some respects, in contrast with Roemmich et al. (2019), who call for a doubling of Argo floats (which includes BGC floats) in the equatorial region. We recommend that BGC Argo managers carefully review the BGC signals they wish to observe before making a significant investment of BGC Argo floats in the western tropical Pacific.

The method employed to draw these conclusions about the optimal BGC float array has limitations: it inherits the biases and uncertainties of the CM4 model on which the prior covariances are based, as well as the narrower set of BGC variables in CM4 compared with BGC Argo; additionally, we only consider four depth levels and use an approximate method to site floats. With more computing power, it would be possible to calculate full-depth eigenvectors and covariances. These estimates only consider spatial covariances and could differ significantly if space and time covariances were used. Finally, sequential algorithms may not be the best way to identify the full array. Alternate algorithms exist that solve for the ideal distribution of floats simultaneously (Hastings 1970) and may offer improvements to the amount of variance the optimal array can constrain, but are computationally more expensive and have not been investigated here.

6. Conclusions

The analysis error covariance $\mathbf{P}^a$ of the existing, future, and uniformly distributed BGC Argo float array has been quantified for the first time, and an optimal BGC Argo array is suggested. We find that the structure of unconstrained variance for the uniformly distributed BGC Argo arrays as well as the May 2021 snapshot both in static form and projected into the future all match the underlying structure of the prior variance: high surface temperature variance in the northern midlatitudes, high surface chlorophyll and salinity variance in the Arctic, and high pH and oxygen variance at 100 m in the northern midlatitudes. We also observe the spatial covariance length scales to be significantly longer at the surface than at depth; this results in subsurface maxima of formal mapping error ($\mathbf{E}^{\mathrm{map}}$) for all variables and may be a result of not using the space-time covariance. The Monte Carlo experiment found that pH and chlorophyll were relatively easy to constrain, and oxygen and salinity were relatively hard to constrain; salinity sensors are already deployed on all core and BGC Argo floats, while reducing oxygen variance may require

additional deployment of oxygen sensors on core Argo floats.

A transition matrix, calculated from all existing Argo trajectories (Chamberlain et al. 2023), was combined with the model CM4 covariances to produce estimates of variance constrained in the future. This prediction was done for the existing full Argo array and also demonstrated the relative variance constrained by two hypothetical floats in the Pacific in the context of surrounding Argo floats. These products and code are now publicly available for use by the broader Argo management community. In addition to an operational tool, we suggest that these maps of current and future Argo array performance are useful for communicating the importance of sustained investment in Argo to both funding agencies and the general public. By specifically quantifying the effectiveness of each float, the impact of each one is less abstract. The next logical step in this research is to translate the unconstrained variance into uncertainty in fluxes or bulk inventories of BGC variables, which would further quantify the direct impacts of BGC Argo observations.

The optimal array experiment identifies the Northern and Southern Hemisphere midlatitudes as the best places to initially deploy BGC Argo floats and as areas that should be prioritized for BGC Argo array maintenance. The western tropical Pacific was identified as a region of low BGC variability, requiring sparser BGC Argo coverage. Comparing the optimal array to random arrays, we found that the optimal array outperformed the random array by 100 floats or 10% on average, corresponding to obtaining equivalent mapping performance with a cost savings of more than $7.5 million over 5 years under current BGC Argo pricing.

As already noted, significant assumptions are made in developing these methods. This work is a first step toward an observations-driven approach to quantifying the effectiveness of present and future BGC Argo arrays.

APPENDIX A

Comparison of Spatial Distribution of Sum of Variances

The result that the western tropical Pacific has less BGC variance is an important result and needs a more expansive treatment than the figures presented in this paper provided. A potential criticism of our methods could be that the scaling σ we have applied to the data [Eq. (17)] has skewed the results. Here we expand the justification.

We begin by showing the time series of the Black Sea, the western tropical Pacific, the eastern tropical Pacific, and the western tropical Atlantic: these regions were selected to show the relative context of global BGC variance (Fig. A1). While salinity variance in the western tropical Pacific is relatively high, temperature, pH, chlorophyll, and oxygen variance are orders of magnitude lower than the other locations considered and the western tropical Pacific combined results are a minimum in BGC variability.
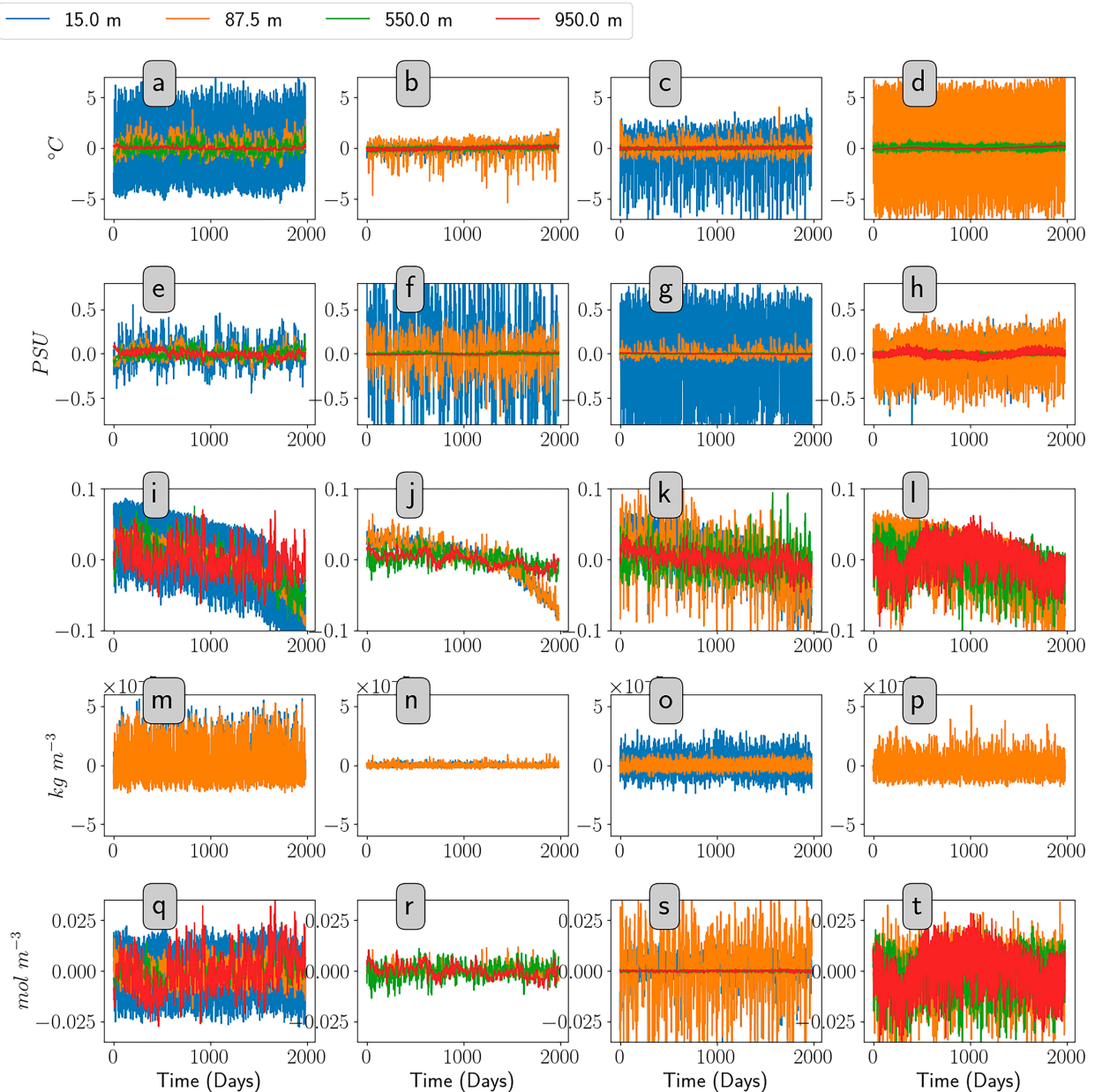

FIG. A1. (a),(e),(i),(m),(q) Raw CM4 time series in the Black Sea (location of very high variance), (b),(f),(j),(n),(m) raw CM4 time series in the western tropical Pacific (location of very low variance of temperature, salinity, pH, chlorophyll, and oxygen, respectively), (c),(g),(k),(o),(s) raw CM4 time series in the eastern tropical Pacific, and (d),(h),(l),(p),(t) raw CM4 time series in the western tropical Atlantic. The mean has been removed from all time series.
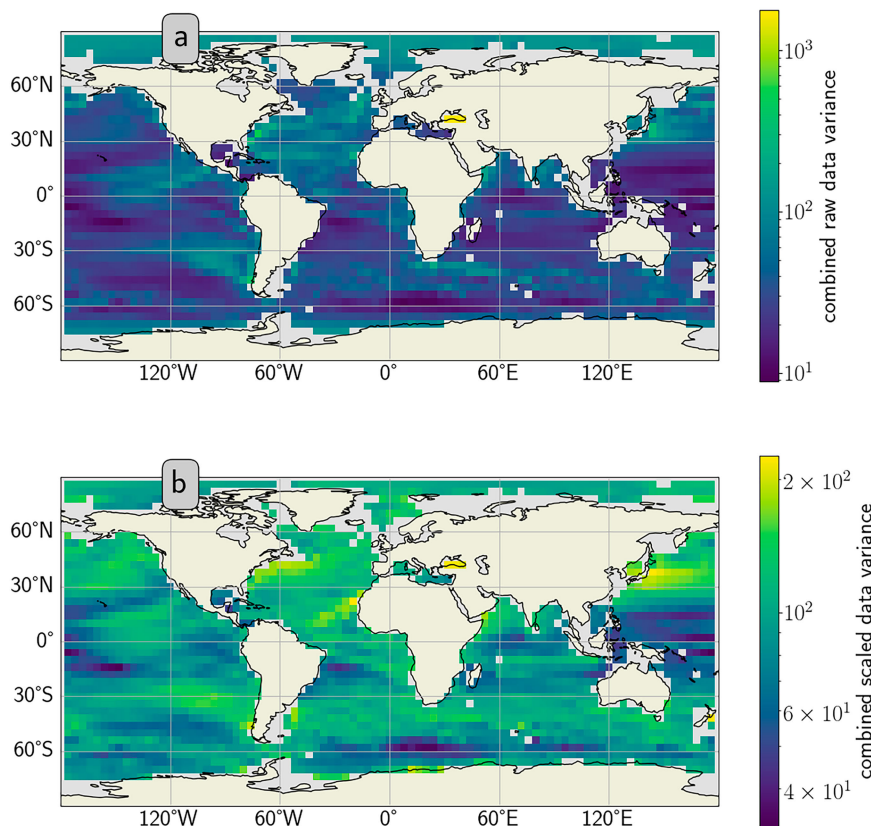
FIG. A2. Sum of total variance at four depth levels considered in optimal array where individual variables are (a) scaled by the median of the temporal standard deviation distribution and (b) scaled as described in Eq. (17).

Scaling biogeochemical data is necessary in order to compare the relative importance of observed variables. Section 6c illustrates that the unnormalized variance covers 10 orders of magnitude from a minimum unnormalized variance of oxygen to a maximum unnormalized variance of temperature. Because of this, if a uniform scaling σ were applied to the data, Eq. (18) will be dominated by surface temperature variance.

Clearly, a nonuniform scaling is necessary, but which is appropriate? To test the scaling used, we consider two alternate cases for σ: First, a scaling that is equal to the minimum or maximum value of the variance of each variable at each depth level and, second, a scaling equal to the median of the variance at each depth level. After some testing (not demonstrated here), we realized that a scaling based on the extremes of the distribution produced suboptimal results, and we defaulted to the median. The field resulting from Eq. (18) with both the median σ and Eq. (17) σ are plotted in Fig. A2. Comparing these two cases, we see that the largest effect of the scaling is to reduce the relative variance in the Black Sea (region of largest variability) and the Arctic (region of second largest variability) (Fig. A2). The reduced BGC variability in the western tropical Pacific is seen in both plots. From this, we can see that Eq. (17) σ reduces

the dynamic range of variability and in so doing highlights a fundamental assumption about our analysis: all of the ocean is biogeochemically important to observe, and no region should be singularly prioritized or ignored. This produces an optimal array that is more uniformly distributed and not concentrated in the Black Sea and boundary currents.

The optimal array algorithm places a float in a location that constrains maximum variance. This is done by finding the maximum absolute value of the sum of the variances [Eq. (18)] of the eigenvector. This is largely controlled by the variance at a grid point and the spatial and intervariable cross covariances. The cross covariances are not obvious and can be significantly greater or smaller than expected. The length scale of spatial covariance appears to be largely informed by variability in the mesoscale eddy structure and front locations. The intervariable cross covariance seems to be largely informed by water mass properties or large-scale physical forcing. The culmination of these two can manifest in unexpected ways, which is why we adopt the eigenvector scheme.

This analysis shows the combined variance in the western tropical Pacific is characteristically low. As this variance is a significant piece of where the algorithm chooses to deploy floats, it is not unreasonable to see an array with few floats deployed in this region.

APPENDIX B

Impact of Scaling on the Data

The raw and scaled data are plotted in Fig. B1. The left side of the figure shows the variance of the raw data from the CM4 model. The right side of the figure shows the variance of the data after it has been scaled. The variance in the unscaled data can cover four orders of magnitude or more. The scaling imposes an artificial democratization where the relative importance of the grid point with the largest variance can, at most, be 15 times greater than the smallest. The scaling was tuned to remove the extremes of the variability distribution while preserving as much signal as possible. All the low variance extremes are removed by setting the minimum scaled variance of the system to the 15th percentile as described in the text. Setting the maximum scaled variance to be a multiple of the lower variance restricts the dynamic range of the variability so that different BGC variables at different depths can be meaningfully compared to one another. Salinity at 550 m is the most impacted by this upper limit with variability artificially capped at the 32nd percentile. The average upper bound over depths and variables exists at the 13th percentile of variances. This choice is not expected to be perfect, and can be adjusted to improve the optimization. The point here is to make the array design and evaluation reproducible.
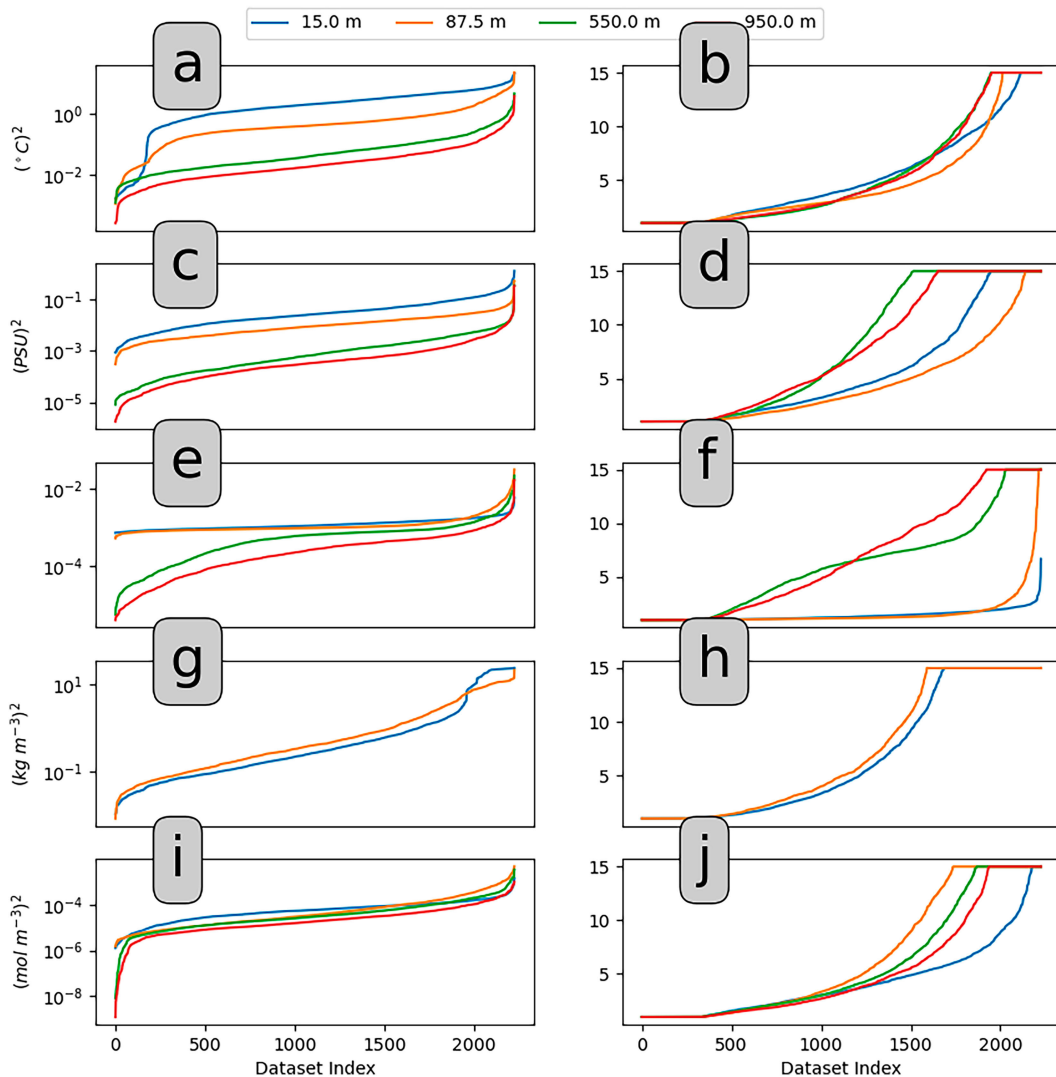

FIG. B1. (a),(c),(e),(g),(i) Raw CM4 data temporal variance and (b),(d),(f),(h),(j) scaled CM4 temporal variance of (top to bottom) temperature, salinity, pH, chlorophyll, and oxygen, respectively. Variance was calculated at each of the four depth levels and sorted from smallest to largest in dataset.

APPENDIX C

Total Variance before Observation

The total variance of the system is determined from the diagonal elements of the background error covariance $\mathbf{P}^b$, prior to observation. The zonally averaged variance of each variable can be seen in Fig. C1.
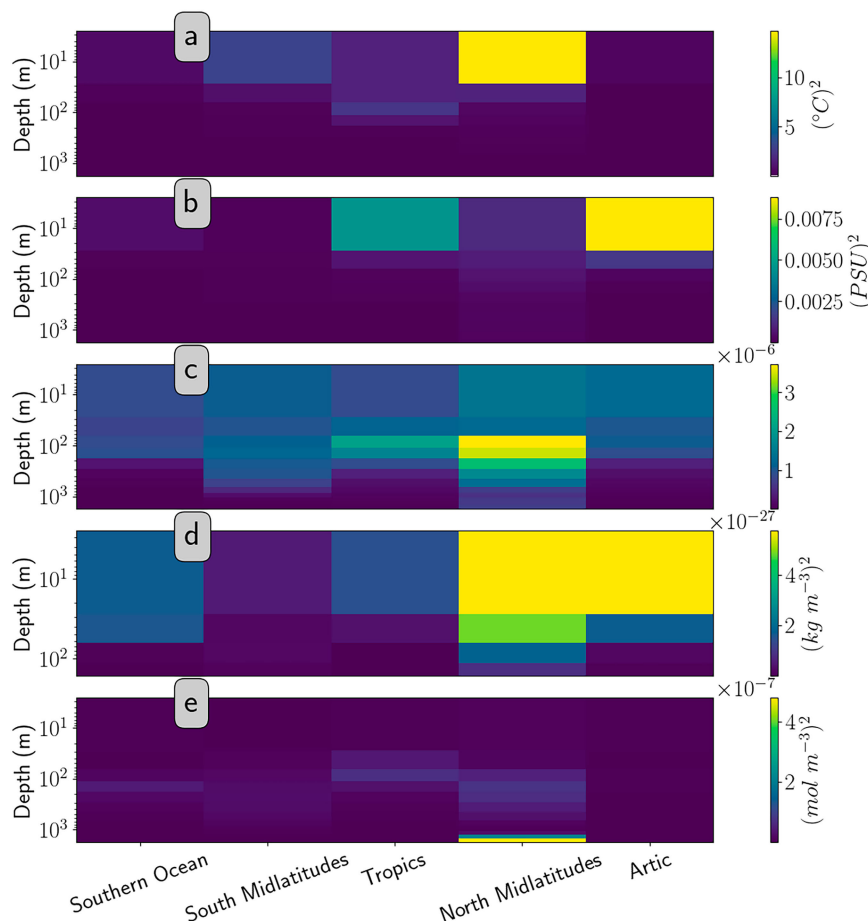

FIG. C1. Zonal average of total variance (diagonal of $\mathbf{P}$) for all variables and depths.

REFERENCES

Adcroft, A., and Coauthors, 2019: The GFDL global ocean and sea ice model OM4.0: Model description and simulation features. *J. Adv. Model. Earth Syst.*, **11**, 3167–3211, https://doi.org/10.1029/2019MS001726.

Argo, 2021: Argo float data and metadata from Global Data Assembly Centre (Argo GDAC)—Snapshot of Argo GDAC of May 10st 2021. SEANOE, accessed 10 November 2022, https://doi.org/10.17882/42182.

Bretherton, F. P., R. E. Davis, and C. B. Fandry, 1976: A technique for objective analysis and design of oceanographic experiments applied to MODE-73. *Deep-Sea Res. Oceanogr. Abstr.*, **23**, 559–582, https://doi.org/10.1016/0011-7471(76)90001-2.

Bushinsky, S. M., A. R. Gray, K. S. Johnson, and J. L. Sarmiento, 2017: Oxygen in the Southern Ocean from Argo floats:

Determination of processes driving air-sea fluxes. *J. Geophys. Res. Oceans*, **122**, 8661–8682, https://doi.org/10.1002/2017JC012923.

——, and Coauthors, 2019: Reassessing Southern Ocean air-sea CO_2 flux estimates with the addition of biogeochemical float observations. *Global Biogeochem. Cycles*, **33**, 1370–1388, https://doi.org/10.1029/2019GB006176.

Cai, W., A. Sullivan, and T. Cowan, 2011: Interactions of ENSO, the IOD, and the SAM in CMIP3 models. *J. Climate*, **24**, 1688–1704, https://doi.org/10.1175/2010JCLI3744.1.

Campbell, E. C., E. A. Wilson, G. W. K. Moore, S. C. Riser, C. E. Brayton, M. R. Mazloff, and L. D. Talley, 2019: Antarctic offshore polynyas linked to Southern Hemisphere climate anomalies. *Nature*, **570**, 319–325, https://doi.org/10.1038/s41586-019-1294-0.

Campbell, J. W., 1995: The lognormal distribution as a model for bio-optical variability in the sea. *J. Geophys. Res.*, **100**, 13 237–13 254, https://doi.org/10.1029/95JC00458.

Chamberlain, P. M., L. D. Talley, M. R. Mazloff, S. C. Riser, K. Speer, A. R. Gray, and A. Schwartzman, 2018: Observing the ice-covered Weddell Gyre with profiling floats: Position uncertainties and correlation statistics. *J. Geophys. Res. Oceans*, **123**, 8383–8410, https://doi.org/10.1029/2017JC012990.

——, ——, ——, E. van Sebille, S. T. Gille, T. Tucker, M. Scanderbeg, and P. Robbins, 2023: Using existing Argo trajectories to statistically predict future float positions with a transition matrix. *J. Atmos. Oceanic Technol.*, **40**, 1083–1103, https://doi.org/10.1175/JTECH-D-22-0070.1.

Dunne, J. P., and Coauthors, 2020: Simple global ocean Biogeochemistry with Light, Iron, Nutrients and Gas version 2 (BLINGv2): Model description and simulation characteristics in GFDL's CM4.0. *J. Adv. Model. Earth Syst.*, **12**, e2019MS002008, https://doi.org/10.1029/2019MS002008.

Fay, A. R., and G. A. McKinley, 2014: Global open-ocean biomes: Mean and temporal variability. *Earth Syst. Sci. Data*, **6**, 273–284, https://doi.org/10.5194/essd-6-273-2014.

Ford, D., 2021: Assimilating synthetic Biogeochemical-Argo and ocean colour observations into a global ocean model to inform observing system design. *Biogeosciences*, **18**, 509–534, https://doi.org/10.5194/bg-18-509-2021.

Galbraith, E. D., A. Gnanadesikan, J. P. Dunne, and M. R. Hiscock, 2010: Regional impacts of iron-light colimitation in a global biogeochemical model. *Biogeosciences*, **7**, 1043–1064, https://doi.org/10.5194/bg-7-1043-2010.

Garcia, H. E., and Coauthors, 2019a: *Dissolved Inorganic Nutrients (Phosphate, Nitrate and Nitrate+Nitrite, Silicate)*. Vol. 4, *World Ocean Atlas 2018*, NOAA Atlas NESDIS 84, 35 pp., https://www.ncei.noaa.gov/sites/default/files/2020-04/woa18_vol4.pdf.

——, and Coauthors, 2019b: *Dissolved Oxygen, Apparent Oxygen Utilization, and Dissolved Oxygen Saturation*. Vol. 3, *World Ocean Atlas 2018*, NOAA Atlas NESDIS 83, 38 pp., https://www.ncei.noaa.gov/sites/default/files/2022-06/woa18_vol3.pdf.

Gaspari, G., and S. E. Cohn, 1999: Construction of correlation functions in two and three dimensions. *Quart. J. Roy. Meteor. Soc.*, **125**, 723–757, https://doi.org/10.1002/qj.49712555417.

Hastings, W. K., 1970: Monte Carlo sampling methods using Markov chains and their applications. *Biometrika*, **57**, 97–109, https://doi.org/10.1093/biomet/57.1.97.

Held, I. M., and Coauthors, 2019: Structure and performance of GFDL's CM4.0 climate model. *J. Adv. Model. Earth Syst.*, **11**, 3691–3727, https://doi.org/10.1029/2019MS001829.

Ide, K., P. Courtier, M. Ghil, and A. C. Lorenc, 1997: Unified notation for data assimilation: Operational, sequential and variational. *J. Meteor. Soc. Japan*, **75**, 181–189, https://doi.org/10.2151/jmsj1965.75.1B_181.

Johnson, K., and H. Claustre, Eds., 2016: The scientific rationale, design, and implementation plan for a Biogeochemical-Argo float array. Biogeochemical-Argo Planning Group, 65 pp., https://doi.org/10.13155/46601.

——, and Coauthors, 2017: Southern Ocean Carbon and Climate Observations and Modeling (SOCCOM) float data archive. UC San Diego Library Digital Collections, accessed 24 October 2022, https://doi.org/10.6075/J0TX3C9X.

Kamenkovich, I., W. Cheng, C. Schmid, and D. E. Harrison, 2011: Effects of eddies on an ocean observing system with profiling floats: Idealized simulations of the Argo array. *J. Geophys. Res.*, **116**, C06003, https://doi.org/10.1029/2010JC006910.

——, A. Haza, A. R. Gray, C. O. Dufour, and Z. Garraffo, 2017: Observing system simulation experiments for an array of autonomous biogeochemical profiling floats in the Southern Ocean. *J. Geophys. Res. Oceans*, **122**, 7595–7611, https://doi.org/10.1002/2017JC012819.

Landschützer, P., N. Gruber, and D. C. E. Bakker, 2016: Decadal variations and trends of the global ocean carbon sink. *Global Biogeochem. Cycles*, **30**, 1396–1417, https://doi.org/10.1002/2015GB005359.

Locarnini, M., and Coauthors, 2018: *Temperature*. Vol. 1, *World Ocean Atlas 2018*, NOAA Atlas NESDIS 81, 52 pp., https://www.ncei.noaa.gov/sites/default/files/2020-04/woa18_vol1.pdf.

Majkut, J. D., B. R. Carter, T. L. Frölicher, C. O. Dufour, K. B. Rodgers, and J. L. Sarmiento, 2014: An observing system simulation for Southern Ocean carbon dioxide uptake. *Philos. Trans. Roy. Soc.*, **A372**, 20130046, https://doi.org/10.1098/rsta.2013.0046.

Markov, A. A., 1906: Rasprostranenie Zakona Bol'shih chisel na velichiny, zavisyaschie drug ot druga (in Russian). *Izv. Fiz.-Mat. Obschestva Kazan. Univ.*, **15**, 135–156.

Mazloff, M. R., P. Heimbach, and C. Wunsch, 2010: An eddy-permitting Southern Ocean state estimate. *J. Phys. Oceanogr.*, **40**, 880–899, https://doi.org/10.1175/2009JPO4236.1.

Monteiro, P. M. S., L. Gregor, M. Lévy, S. Maenner, C. L. Sabine, and S. Swart, 2015: Intraseasonal variability linked to sampling alias in air–sea CO_2 fluxes in the Southern Ocean. *Geophys. Res. Lett.*, **42**, 8507–8514, https://doi.org/10.1002/2015GL066009.

NASA, 2022: Ocean Biology Processing Group, AOB. OB.DAAC, accessed 27 June 2022, https://oceancolor.gsfc.nasa.gov/.

Prend, C. J., S. T. Gille, L. D. Talley, B. G. Mitchell, I. Rosso, and M. R. Mazloff, 2019: Physical drivers of phytoplankton bloom initiation in the Southern Ocean's Scotia Sea. *J. Geophys. Res. Oceans*, **124**, 5811–5826, https://doi.org/10.1029/2019JC015162.

Reygondeau, G., A. Longhurst, E. Martinez, G. Beaugrand, D. Antoine, and O. Maury, 2013: Dynamic biogeochemical provinces in the global ocean. *Global Biogeochem. Cycles*, **27**, 1046–1058, https://doi.org/10.1002/gbc.20089.

Roemmich, D., and J. Gilson, 2009: The 2004–2008 mean and annual cycle of temperature, salinity, and steric height in the global ocean from the Argo program. *Prog. Oceanogr.*, **82**, 81–100, https://doi.org/10.1016/j.pocean.2009.03.004.

——, and Coauthors, 1999: On the design and implementation of Argo: A global array of profiling floats. Argo Science Team Doc., 35 pp., https://argo.ucsd.edu/wp-content/uploads/sites/361/2020/05/argo-design.pdf.

——, and Coauthors, 2019: On the future of Argo: A global, full-depth, multi-disciplinary array. *Front. Mar. Sci.*, **6**, 439, https://doi.org/10.3389/fmars.2019.00439.

Saxon, 2008: *Saxon Algebra 2*. Houghton Mifflin Harcourt, 1048 pp.

Schlunegger, S., and Coauthors, 2020: Time of emergence and large ensemble intercomparison for ocean biogeochemical trends. *Global Biogeochem. Cycles*, **34**, e2019GB006453, https://doi.org/10.1029/2019GB006453.

Sévellec, F., A. Colin de Verdiére, and M. Ollitrault, 2017: Evolution of intermediate water masses based on Argo float displacements. *J. Phys. Oceanogr.*, **47**, 1569–1586, https://doi.org/10.1175/JPO-D-16-0182.1.

Talley, L. D., V. Lobanov, V. Ponomarev, A. Salyuk, P. Tishchenko, I. Zhabin, and S. Riser, 2003: Deep convection and brine rejection in the Japan Sea. *Geophys. Res. Lett.*, **30**, 1159, https://doi.org/10.1029/2002GL016451.

Zweng, M. M., and Coauthors, 2019: *Salinity*. Vol. 2, *World Ocean Atlas 2018*, NOAA Atlas NESDIS 82, 50 pp., https://www.ncei.noaa.gov/sites/default/files/2022-06/woa18_vol2.pdf.